



# **NAVAL POSTGRADUATE SCHOOL**

**MONTEREY, CALIFORNIA**

## **THESIS**

### **OPTICAL READOUT SYSTEM FOR BI-MATERIAL TERAHERTZ SENSORS**

by

Elison Montagner

September 2011

Thesis Advisor:

Associate Advisor:

Second Reader:

Dragoslav Grbovic

David C. Jenn

Fabio D. P. Alves

**Approved for public release; distribution is unlimited**

THIS PAGE INTENTIONALLY LEFT BLANK

<b>REPORT DOCUMENTATION PAGE</b>			<i>Form Approved OMB No. 0704-0188</i>	
Public reporting burden for this collection of information is estimated to average 1 hour per response, including the time for reviewing instruction, searching existing data sources, gathering and maintaining the data needed, and completing and reviewing the collection of information. Send comments regarding this burden estimate or any other aspect of this collection of information, including suggestions for reducing this burden, to Washington headquarters Services, Directorate for Information Operations and Reports, 1215 Jefferson Davis Highway, Suite 1204, Arlington, VA 22202-4302, and to the Office of Management and Budget, Paperwork Reduction Project (0704-0188) Washington DC 20503.				
<b>1. AGENCY USE ONLY (Leave blank)</b>		<b>2. REPORT DATE</b> September 2011	<b>3. REPORT TYPE AND DATES COVERED</b> Master's Thesis	
<b>4. TITLE AND SUBTITLE</b> Optical Readout System for Bi-Material Terahertz Sensors			<b>5. FUNDING NUMBERS</b>	
<b>6. AUTHOR(S)</b> Elison Montagner				
<b>7. PERFORMING ORGANIZATION NAME(S) AND ADDRESS(ES)</b> Naval Postgraduate School Monterey, CA 93943-5000			<b>8. PERFORMING ORGANIZATION REPORT NUMBER</b>	
<b>9. SPONSORING /MONITORING AGENCY NAME(S) AND ADDRESS(ES)</b> N/A			<b>10. SPONSORING/MONITORING AGENCY REPORT NUMBER</b>	
<b>11. SUPPLEMENTARY NOTES</b> The views expressed in this thesis are those of the author and do not reflect the official policy or position of the Department of Defense or the U.S. Government. IRB Protocol number NA.				
<b>12a. DISTRIBUTION / AVAILABILITY STATEMENT</b> Approved for public release; distribution is unlimited			<b>12b. DISTRIBUTION CODE</b> A	
<b>13. ABSTRACT (maximum 200 words)</b>  The objective of this work is to design, assemble, and characterize an optical readout for bi-material MEMs sensor arrays that can be integrated into a THz imaging system. All this effort is a contribution to the goals of the research conducted by the Naval Postgraduate School Sensor Research Laboratory on designing and fabricating THz-optimized bi-material MEMs sensor arrays for THz imaging. Basic concepts of THz radiation and detection are presented. Several aspects of THz imaging, and sensor's array readout possibilities, are discussed in terms of the principle of operation for this type of sensor. An experimental optical readout was assembled during this research, and its configuration is shown, as well as all of its component details. The experimental setup was characterized following a method described in this work, and the obtained results are analyzed. Finally, one possibility of optical readout integration with a THz imaging system is suggested.				
<b>14. SUBJECT TERMS</b> Optical Readout, Terahertz, Sensor Array, Bi-material MEMs, Imaging			<b>15. NUMBER OF PAGES</b> 99	
			<b>16. PRICE CODE</b>	
<b>17. SECURITY CLASSIFICATION OF REPORT</b> Unclassified	<b>18. SECURITY CLASSIFICATION OF THIS PAGE</b> Unclassified	<b>19. SECURITY CLASSIFICATION OF ABSTRACT</b> Unclassified	<b>20. LIMITATION OF ABSTRACT</b> UU	

THIS PAGE INTENTIONALLY LEFT BLANK

**Approved for public release; distribution is unlimited**

**OPTICAL READOUT SYSTEM FOR BI-MATERIAL TERAHERTZ SENSORS**

Elison Montagner  
Lieutenant Colonel, Brazilian Air Force  
B.S., Brazilian Air Force Academy, 1991

Submitted in partial fulfillment of the  
requirements for the degree of

**MASTER OF SCIENCE IN ELECTRONIC WARFARE SYSTEMS  
ENGINEERING**

from the

**NAVAL POSTGRADUATE SCHOOL  
September 2011**

Author: Elison Montagner

Approved by: Dragoslav Grbovic, PhD  
Thesis Advisor

David C. Jenn, PhD  
Associate Advisor

Fabio D. P. Alves, PhD  
Second Reader

Dan Boger, PhD  
Chair, Department of Information Science

THIS PAGE INTENTIONALLY LEFT BLANK

## **ABSTRACT**

The objective of this work is to design, assemble, and characterize an optical readout for bi-material MEMs sensor arrays that can be integrated into a THz imaging system. All this effort is a contribution to the goals of the research conducted by the Naval Postgraduate School Sensor Research Laboratory on designing and fabricating THz-optimized bi-material MEMs sensor arrays for THz imaging. Basic concepts of THz radiation and detection are presented. Several aspects of THz imaging, and sensor's array readout possibilities, are discussed in terms of the principle of operation for this type of sensor. An experimental optical readout was assembled during this research, and its configuration is shown, as well as all of its component details. The experimental setup was characterized following a method described in this work, and the obtained results are analyzed. Finally, one possibility of optical readout integration with a THz imaging system is suggested.

THIS PAGE INTENTIONALLY LEFT BLANK



# TABLE OF CONTENTS

I.	INTRODUCTION.....	1
A.	TERAHERTZ IMAGING SYSTEMS.....	2
1.	THz Radiation.....	2
2.	Detecting Terahertz .....	4
3.	Imaging Systems for THz .....	7
4.	Sensor Readout Techniques in THz Imaging Systems .....	8
II.	BI-MATERIAL THZ SENSOR ARRAY .....	11
A.	PRINCIPLE OF OPERATION .....	11
B.	SENSOR STRUCTURE .....	14
C.	SENSOR COMPONENTS.....	15
D.	OPTICAL READOUT FOR BI-MATERIAL SENSORS.....	17
1.	Concept .....	17
2.	Multiple-Sensor-Probing Configuration.....	17
3.	Optical Readout Limitations .....	19
III.	DESIGN AND ASSEMBLY OF OPTICAL READOUT SIMULTANEOUSLY PROBING MULTIPLE DETECTORS .....	21
A.	GENERAL DESCRIPTION .....	21
B.	READOUT SUBSYSTEMS .....	23
1.	Light Source.....	23
2.	Lenses and Aperture Control .....	26
3.	Sensor Vacuum Chamber .....	29
4.	CCD Camera.....	31
C.	CAMERA SOFTWARE CONTROL.....	33
1.	General Design .....	33
a.	<i>Camera Setup</i> .....	34
b.	<i>Background Image Frame Acquisition</i> .....	35
c.	<i>Sequential Image Frame Acquisition</i> .....	35
d.	<i>Subtracted Image Display</i> .....	36
e.	<i>Image Edge Detection</i> .....	36
2.	Front Panel .....	38
3.	Block Diagram.....	42
IV.	OPTICAL READOUT CHARACTERIZATION.....	45
A.	SETUP RESOLUTION ESTIMATION METHOD .....	45
1.	Sensor Characterization.....	47
a.	<i>Procedure</i> .....	47
b.	<i>Results</i> .....	49
2.	Readout Characterization .....	52
a.	<i>Procedure</i> .....	52
b.	<i>Results</i> .....	53
B.	READOUT ANALYSIS.....	55

C.    OPTICAL READOUT AND THZ IMAGING SYSTEM INTEGRATION.....	56
V.    CONCLUSIONS.....	59
LIST OF REFERENCES.....	61
APPENDIX A. CAMERA CONTROLS AND IMAGE ANALYSIS SOFTWARE PROCESSES FLOWCHARTS .....	67
APPENDIX B. APPLICATION SOFTWARE HMI.....	73
APPENDIX C. APPLICATION BLOCK DIAGRAM .....	75
INITIAL DISTRIBUTION LIST .....	79

## LIST OF FIGURES

Figure 1.	Spectrum of electromagnetic radiation with emphasis on THz range between microwaves and infrared. After [2].	2
Figure 2.	Output average power ranges of THz sources at specific frequency ranges. The highlighted areas in the graph represent the output average of the following sources: 1-Photoconductive Antenna (PCA); 2-Optical Rectification (OR); 3-CO <sub>2</sub> laser frequency mixing; 4-Difference-Frequency Generation (DFG); 5-Optically pumped laser; 6-Quantum Cascade Laser (QCL); 7-p-Type Germanium Laser (p-Ge-laser). From [4].	3
Figure 3.	Illustration of a sensor designed with bi-material structure and multifold legs supporting the resonant cavity. From [13].	11
Figure 4.	Schematics of the transmission illumination technique wherein an image is formed by the shadow of radiation.	13
Figure 5.	Schematics of the reflection illumination technique wherein an image is formed by the radiation reflected from the object.	13
Figure 6.	Part of a sensor array and an enlarged view of one isolated sensor with highlights on the regions of its structure. After [10]	14
Figure 7.	Bi-material sensor structure (dimensions in $\mu\text{m}$ ). After [38]	15
Figure 8.	Material distribution over the pixel's structure. After [38]	16
Figure 9.	Schematic example of multiple-sensor probing using one light beam to illuminate all sensors in the array, and the reflections from all sensors captured by a CCD camera simultaneously. From [10]	18
Figure 10.	Architectural design for optical readout for probing multiple detectors.	21
Figure 11.	Diagram showing aperture blocking reflected rays coming from deflected sensor.	22
Figure 12.	Cree XLamp XP-E LED Green: used as the visible light source for the readout. From [43]	23
Figure 13.	Light source subsystem scheme shows how the beam emitted by the LED is controlled by the aperture in order to illuminate the complete area of the Lens 1.	24
Figure 14.	Light source subsystem photo showing the components assembled in the laboratory.	25
Figure 15.	Lenses and aperture control sub-system showing Lens 2 controlling the convergence of the beam to Aperture Control 2, and Lens 3 forming image into the CCD.	27
Figure 16.	Top-view picture of the lenses and aperture control subsystem assembled in laboratory.	28
Figure 17.	Transmission spectra of tsurupica and polyethylene in THz spectral range with the area of interest for this work highlighted. After [44]	30

Figure 18.	Picture of the vacuum chamber on a rotating mount from the window for the visual range side. The sensor array can be observed inside the chamber. ....	31
Figure 19.	Graph of quantum efficiency for CCD camera Basler A631f with the maximum quantum efficiency highlighted (dashed blue) at around 525nm of wavelength. After [47].....	33
Figure 20.	High-level application flowchart. ....	34
Figure 21.	Camera setup HMI. ....	39
Figure 22.	Files setup HMI.....	39
Figure 23.	Background and actual image information displays.....	40
Figure 24.	Simple and absolute subtraction images displays and histograms.....	40
Figure 25.	Image area selection control HMI. ....	41
Figure 26.	Area selection and display analysis tools HMI.....	41
Figure 27.	Image edge detection tools and displays HMI. ....	42
Figure 28.	Picture of the array used in the characterization method proposed in this work. It has 120 x 120 sensors. After [13].....	45
Figure 29.	Picture of an HT10K Foil Heater produced by Minco Co., used to control the temperature of the sensor during the characterization procedure. From [52].....	46
Figure 30.	Setup used to control the temperature over the sensor array. The sensor array can be observed fixed on the copper plate that is wired to the power source and the multimeter. The multimeter monitors the heater temperature. ....	47
Figure 31.	Sensor's dimensions and indication of the measured Key Points position. The difference between the heights of both indicated points provides the angular displacement of the resonant cavity. After [38].....	48
Figure 32.	Sensor Characterization setup scheme. The microscope is used to measure the distance between the microscope lens and the key points over the resonant cavity; the difference between these two distances, divided by the resonant cavity length, gives the sensor's angular deflection at a given temperature. ....	49
Figure 33.	Plot of data from Sensor Characterization procedure. Each line on the plot represents a linear fit over the data obtained from each sensor. A very similar angular deflection per unit Kelvin between the measured sensors can be observed.....	50
Figure 34.	Data regression from the sensor characterization procedure where common behavior parameters are computed for all data. ....	51
Figure 35.	Plot of data from readout-characterization procedure. Each solid line on the plot represents a linear fit over the data obtained from each sensor. A very similar behavior between two sensors analyzed can be observed.....	53
Figure 36.	Data regression from readout characterization procedure where common behavior parameters are computed for all data. ....	54

Figure 37.	THz Imaging System setup scheme being developed in the NPS Sensor Laboratory. After [13]. .....	56
Figure 38.	Camera setup process. ....	67
Figure 39.	Background image frame acquisition process. ....	68
Figure 40.	Sequential image frames acquisition process. ....	69
Figure 41.	Subtracted images displaying process. ....	70
Figure 42.	Image edges detection process.....	71
Figure 43.	Software application front panel. ....	73
Figure 44.	First sub-block diagram. ....	75
Figure 45.	Second sub-block diagram. ....	76
Figure 46.	Third sub-block diagram. ....	77
Figure 47.	Fourth sub-block diagram.....	78

THIS PAGE INTENTIONALLY LEFT BLANK

## LIST OF TABLES

Table 1.	Spatial filters available in the application. After [50] .....	37
Table 2.	Camera setup used in the readout. ....	38
Table 3.	Software application block diagram summary description. ....	43

THIS PAGE INTENTIONALLY LEFT BLANK



## LIST OF ACRONYMS AND ABBREVIATIONS

ADC	Analog to Digital Converter
AFM	Atomic Force Microscopy
AVI	Audio Video Interleave
BMP	Bitmap Image File
CCD	Charged-Coupled Device
DFG	Difference-Frequency Generation
FOV	Field of View
FPA	Focal Plane Array
fps	Frames Per Second
FTIR	Fourier Transform Infrared
HMI	Human-Machine Interface
IR	Infrared
KEFO	Knife-Edge Filter Operation
lm	Lumens
MEMS	Microelectromechanical System
NPS	Naval Postgraduate School
NTC	Negative Temperature Coefficient
OR	Optical Rectification
PCA	Photoconductive antenna
PDA	Photoconductive Dipole Antenna
p-Ge-laser	p-Type Germanium Laser
QCL	Quantum Cascade Laser
ROIC	Readout Integrated Circuit
SNR	Signal-to-Noise Ratio
TDS	Time–Domain Spectroscopy
THz	Terahertz Time
THz-TDS	Terahertz Time–Domain Spectroscopy
VGC	Variable Gain Control

THIS PAGE INTENTIONALLY LEFT BLANK

## **ACKNOWLEDGMENTS**

I would like to express my gratitude to:

The Brazilian Air Force for investing in technical and operational postgraduate programs.

Coronel Aviador Fabio Durante Pereira Alves, of the Brazilian Air Force, for his friendship, guidance, trust, and support.

Professor Gamani Karunasiri for his friendship, and confidence.

Professor David C. Jenn for his confidence, and guidance.

Mr. Samuel Barone for his friendship and unconditional laboratory support.

The Naval Postgraduate School's International Program Office, especially Colonel USMC (Ret.) H. Gary Roser, for making my stay at NPS gainful and pleasant.

My Naval Postgraduate friends and partners from all countries and disciplines for the daily encouragement and support.

Professor Dragoslav Grbovic for his friendship, wisdom, and guidance that made possible the accomplishments of this work.

My wife, Angela, for the sacrifice, patience, support, and love throughout this challenge.

THIS PAGE INTENTIONALLY LEFT BLANK

## I. INTRODUCTION

In recent years, terahertz (THz) imaging has been gaining increasing attention because of its many distinctive properties. The radiation is non-ionizing and hence favorable to applications seeking human exposure, especially medical diagnosis and security screening. Several materials, including some explosive constituents, display unique THz absorption patterns [1] and are therefore detectable by THz detectors.

Currently, the Sensor Research Laboratory at Naval Postgraduate School (NPS) is conducting research on design and fabrication of THz-optimized bi-material Microelectromechanical System (MEMS) sensor arrays for THz imaging. Part of this effort focuses on a readout system to quantify sensor arrays' responses, and it is this aspect the current work addresses.

Chapter II focuses on bi-material THz sensor arrays and presents their principle of operation and the architectural design for the sensor array that is referenced for this work.

Chapter III presents the concept for an optical readout for bi-material sensors found in the literature, and the multiple sensors–probing configuration is explained, as well as the limitations of this technique.

After the theoretical discussion, Chapter IV details the multiple-sensors-probing optical readout designed and assembled for this work, showing its subsystems, hardware components, and the Charged-Coupled Device (CCD) camera software control specifically developed to provide tools to analyze generated images.

A methodology to estimate the ability of the readout to produce different pixel brightness for sensors with different angles of deformation (readout resolution) is established and described in Chapter V. Obtained results are presented and analyzed, and the integration of the optical readout in a THz imaging system is discussed.

Finally, concluding remarks are presented. Potential methods to improve the readout characteristics not addressed in this work are suggested for future work.

## A. TERAHERTZ IMAGING SYSTEMS

Terahertz imaging systems are intended to be sensitive to variations in THz radiation emitted by targets of interest and thus to allow observation of that information in the form of an image. A definition of THz radiation itself is necessary to better understand aspects of this imaging process.

### 1. THz Radiation

*Terahertz radiation* refers to sub-millimeter wave energy that fills the range between microwaves and infrared. The region below 1 THz was frequently referred to as part of the world of electronics, and the region of higher frequencies to the world of optics, as depicted in Figure 1. In fact, the THz radiation is difficult to access using either conventional optical methods or classical electronic devices due to the absence of powerful sources [2].

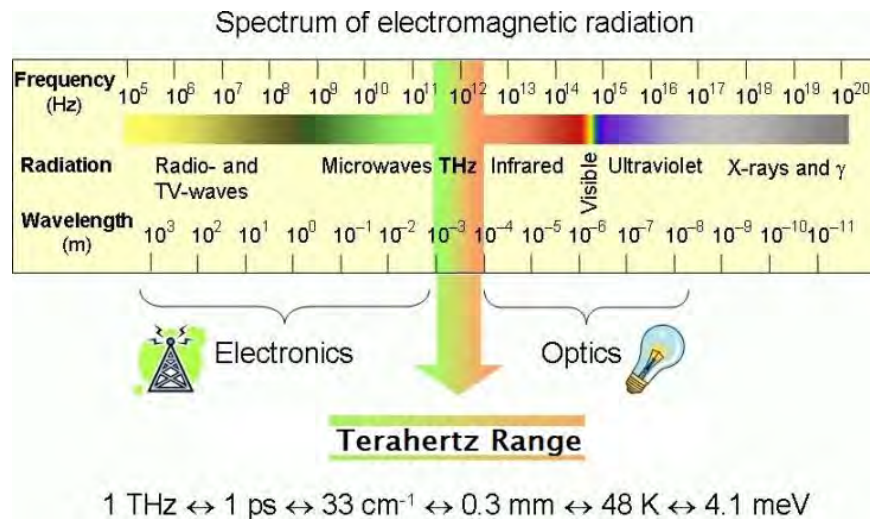
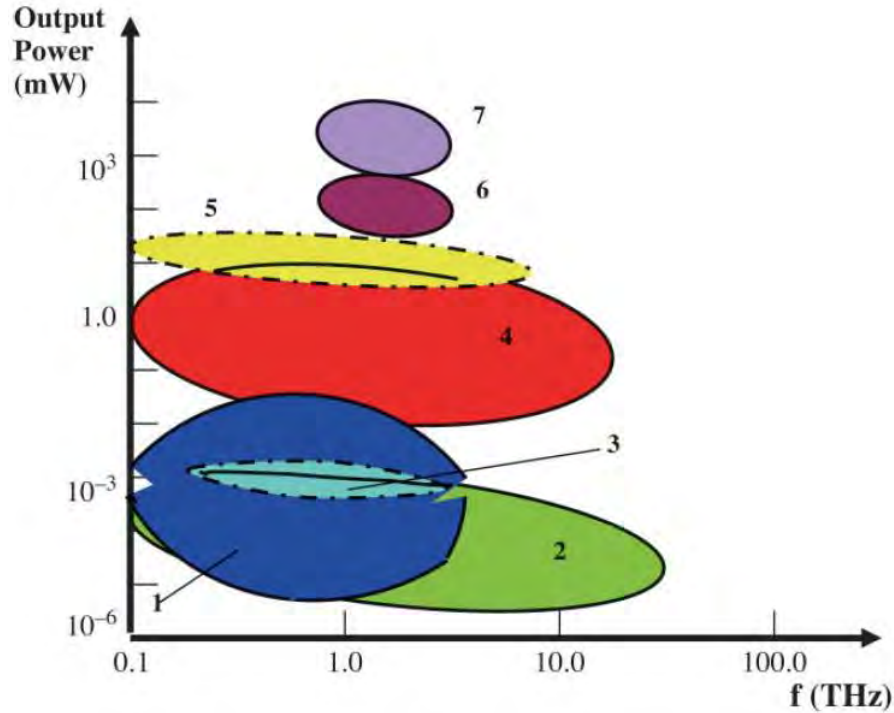


Figure 1. Spectrum of electromagnetic radiation with emphasis on THz range between microwaves and infrared. After [2].

Terahertz radiation is emitted by any object as “black-body radiation,” but the total intensity emitted at all frequencies is less than one millionth of a watt per square centimeter [3], so it is a very weak emission. For imaging systems, higher power radiation is better suited for less sensitive sensors. In Figure 2, the output power of most of the THz sources in operation today, which are attractive for science, medicine, imaging, and engineering applications, can be seen [4].



1-PCA; 2-OR; 3-CO<sub>2</sub> laser frequency mixing;

4-DFG; 5-optically pumped laser; 6-QCL; 7- p-Ge-laser.

Figure 2. Output average power ranges of THz sources at specific frequency ranges. The highlighted areas in the graph represent the output average of the following sources: 1-Photoconductive Antenna (PCA); 2-Optical Rectification (OR); 3-CO<sub>2</sub> laser frequency mixing; 4-Difference-Frequency Generation (DFG); 5-Optically pumped laser; 6-Quantum Cascade Laser (QCL); 7-p-Type Germanium Laser (p-Ge-laser). From [4].

In contrast to X-rays, waves in the THz range have less energy and cannot “ionize” cellular atoms, thus avoiding the damage to living tissue that can

lead to radiation sickness or cancer. Therefore, people exposed to such radiation will not suffer harmful effects [5]. Terahertz radiation can pass through clothing, paper, cardboard, wood, masonry, plastic, ceramics, fog, and clouds, but cannot penetrate metal or water [6]. These properties make THz a good option for security inspection applications, since THz absorption patterns could not only detect but also help in identifying a wider variety of hazardous or illegal substances. For example, “Extensive studies have shown that illegal drugs and explosives can be identified from their THz spectra and prototype systems are already in place in Japan to scan mail online as it passes through the automated systems” [7].

Many applications of radiation in the THz range were described by Siegel [8], mainly for astronomy, the military, and medicine. An important possible application enables doctors to better detect and treat certain types of cancer and dentists to image teeth in a safer way [5]. THz spectroscopy and imaging techniques are also attractive for chemical and industrial applications [9]. The latest developments in bi-material-based MEMS uncooled infrared (IR) imaging technology [10] promise the possibility of their use in real-time THz imaging.

## **2. Detecting Terahertz**

Several types of detectors can be used to detect THz radiation. Detection techniques in the THz range may be classified as either *coherent* or *incoherent*. Basically, coherent detection measures the amplitude and phase of the field, and incoherent detection measures the intensity [11], which is usually the case in MEMS sensor arrays.

Common MEMS sensors used to detect THz are the microbolometers. Microbolometer Focal Plane Arrays (FPA) are based on the thermoresistance effect. Vanadium oxides (VOx) and amorphous silicon are examples of thermoresistant materials currently in use. Cameras with microbolometers, which have good sensitivity at lower costs and which work at room temperature, have



been developed for IR and THz high-speed imaging. The microbolometer has been reported as a powerful tool for terahertz imaging, in both transmission and reflection modes [12].

The fabrication of microbolometer FPAs is relatively complex due to the required monolithic integration of readout electronics with the MEMS pixel. An alternative to microbolometers are the bi-material MEMS FPAs using optical readouts that simplify the FPA fabrication process by decoupling readout and sensing [13]. This type of detector is the object of this work and will be detailed in Chapter II.

Another THz type of detector is the pyroelectric, which is an AC thermal detector that works at room temperature and has a broad and flat spectral response across most of the electronic spectrum. It is based on ferroelectric crystals (i.e.,  $\text{LiTaO}_3$ ), which have a pyroelectric effect that is a pronounced thermal effect. It can be sensitive at frequencies between 0.1 to 3000 THz. [14]

The Golay cell was invented in 1947. It is an opto-acoustic detector, operates at room temperature, and is sensitive, with good efficiency, in the spectral range from 0.02 to 20 THz [15]. Good transmission results were reported by Hübers [16] using 1.6 THz, and when measured with a gas laser and a Golay detector.

Photoconductive dipole antennas (PDA) can be THz detectors fabricated as micro-striplines or coplanar transmission lines on photoconductive inorganic substrates to be used in an optoelectronic technique to detect THz. They have excellent sensitivity and a smooth frequency response, but a narrow usable bandwidth [17], [18], [19]. On the other hand, the optical technique uses electro-optical sampling for detection with good sensitivity and a large bandwidth. The electro-optic effect is a nonlinear coupling between a low frequency electric field (THz pulse) and a laser beam (optical pulse) in a sensor crystal. It is attractive because it can provide a flat frequency spectrum and a true cross-correlation signal [17], [20].

Organic materials are another option for generation and detection of broadband THz radiation. For all-optical and optoelectronic techniques, they show great potential and broaden the material possibilities. Amorphous electro-optical polymers and organic electro-optical crystals are examples of materials reported by Zheng et al. [17] and Scheneider et al. [21] as used for detection.

Fourier transform spectroscopy is a technique that can use THz detectors measuring the radiation that is reflected or passed through a sample, resulting in the spectrum that represents the molecular absorption and transmission, or the molecular fingerprint, of the sample [22].

The THz time-domain spectroscopy (THz-TDS) is another technique that uses a femtosecond laser producing a pulse train that is divided in two: one part is used to produce the THz radiation and the other is used to gate a detector. At the detector, the THz electric field is sampled at various delays relative to the arrival of the THz pulse at the detection point. Achieving accurate results relies on precise synchronization between the femtosecond optical pulse and the THz pulse, to provide a direct measurement of the THz electric field, not merely its intensity [23]. THz-TDS has advantages at frequencies lower than 3 THz, whereas Fourier transform spectroscopy works better at frequencies above 5 THz [24].

Radiation detection can be done from a single spot or from wide areas. To do spot detection, the use of one detector should be enough. Scanning wider areas, detectors can be combined with scanning optical components in order to image such areas. Another option for imaging is combining multiple detectors in a grid, or array, placed in the optical component's focal plane, where the image of an object forms. A combination of multiple detectors in grids is widely known as a Focal Plane Array.

If it is necessary to not only detect THz radiation, but also to show an image of objects, detectors and imaging techniques have to work together in systems designed for this objective.

### **3. Imaging Systems for THz**

Imaging systems can receive and convert information emanated by targets placed inside the field of view (FOV). Depending on the application of the system, the extracted information should be converted into formats for applications with commercial photograph cameras, bar code scanners, or machine vision systems.

Since THz radiation arises from any natural source, it is possible to image such sources passively. A passive THz imaging system was reported in 2002 using a 16-pixel chip. After that, several systems were produced and are in use in airports, ports, public transport facilities, military installations and other high-security sites. Because passively emitted THz signals are so weak, it is difficult to develop systems working at high acquisition rates. As an example, reported in 2009, a system could take about 20 minutes to create a single 40 x 40 pixel image [25].

To become independent of the weak natural THz radiation, active imaging systems can employ artificial external illumination sources. The first images obtained in this way were reported in 1995, by Hu and Nuss [26]. Since then, the high interest in applying the technology for healthcare and security purposes has led to new developments. These systems can operate in either reflection or transmission mode (detailed in Chapter II), and applications in aerospace, homeland security, defense, and healthcare have been reported. The possibility of using high-powered sources of THz can allow the use of conventional and less costly detectors [25]. For this purpose, MEMS sensor arrays have been considered a good choice [10].

However, efficient imaging in the THz range is still a challenge. Considering the difficulties in developing techniques with more sensitive THz detection and better delivery of THz signals to a physical area of concern, actual THz techniques could be heading for use in more detailed identification of specific targets rather than for use as the first-line source of detection [7].

Using MEMS for imaging, each singular sensor usually designates a single point in a raster image or the smallest addressable screen element in a display device. Each sensor should have a proportional reaction to the absorbed amount of THz radiation. If this reaction is converted to information, that information should be enough to recreate an image of the target. For that recreation, an adequate readout has to be used.

#### **4. Sensor Readout Techniques in THz Imaging Systems**

The readout techniques of some sensors have already been demonstrated, e.g., capacitive [27], piezoresistive [28], electron tunneling [29], and optical [30], [31].

In capacitive readout, the capacitance of the pixel varies according to the deformation of the top plate of the capacitor caused by the temperature variance in the sensor. The capacitance is read electronically from physical connections to each pixel [27]. At least five types of noise are present in capacitive readout [10].

Oden et al. [28] demonstrated the use of a piezoresistive cantilever for imaging, moving that cantilever along the focal plane of a set of lenses where an IR image was forming. The position of the cantilever was controlled with a bi-axis translation stage and the response of the cantilever was displayed using a lock-in amplifier. In a piezoresistive detector, two electrodes are connected to two deformable temperature-sensitive legs. Monitoring the current passing through the legs makes it possible to measure its deformation as the resistance changes following temperature changes [10].

In the electron tunneling technique, the information from each pixel comes from the variation of the capacitance of a membrane that is deformed by IR energy. The thermodynamics of the sensor's structure are very important for obtaining good results from this technique [29].

The optical readout technique permits a contactless readout of FPAs without any microelectronic circuitry. Therefore, it is easily scalable to larger

arrays, has the simplicity of optical probing, and has a potential for high yield and low cost [32]. It can measure all sensor deflections simultaneously with high resolution and display the information in a human-eye-readable format. One of the advantages is the possibility of reading signals from all of the array's sensors instead of scanning each one, and maintaining high sensitivity with low crosstalk [31].

By using an external optical readout, it is possible to make the fabrication of MEMS sensor arrays much easier than conventional microbolometer focal plane arrays, since no readout electronics need to be integrated. Salerno [33] reports the optical readout technique as the most effective in cost and sensitivity for large-arrays sensors. The optical readout method brings such advantages as simple fabrication at lower costs, no need of a readout integrated circuit (ROIC) and consequently avoidance of parasitic heat conduction. Furthermore, it can scan of all the array's sensors at same time by the CCD camera, and elimination of thermal leakage caused by electrical conductors in contact with the sensor. This method separates the sensor and readout. The separation allows the bi-material sensors to operate passively and potentially enables operation near the theoretical limit [33].

Considering all the characteristics and advantages of the optical readout technique for extracting information from MEMS sensor arrays working in the THz range, the research group of the NPS Research Sensor Laboratory established this technique as the first one to investigate and test along with the THz sensor fabrication and characterization process.

In this context, and as a contribution to the goals of that research, **the objective of this work is the design, assembly, and characterization of an optical readout for bi-material MEMS sensor arrays capable of being integrated into a THz imaging system.**

To design and implement the readout, it is necessary to understand how the structure works and what its characteristics are. In the following chapter, the construction and general aspects of the MEMS sensor array used as reference for this work are described.

## II. BI-MATERIAL THZ SENSOR ARRAY

The bi-material MEMS THz sensor array is the core of a THz imaging system, wherein the received radiation is converted to easily readable information.

Bi-material sensor arrays can be constructed using suspended microcantilevers (microstructures) with bi-material regions, as illustrated in Figure 3. This sensor design provides direct conversion of absorbed heat into a mechanical response. Such sensors can be referred to as thermo-mechanical detectors [34].

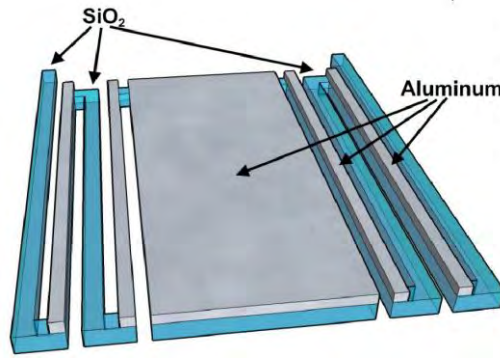


Figure 3. Illustration of a sensor designed with bi-material structure and multifold legs supporting the resonant cavity. From [13]

The design of each sensor structure is very important. Each sensor has to be strong enough to remain suspended and sufficiently flexible to permit its reaction in moving according to the absorbed radiation.

### A. PRINCIPLE OF OPERATION

As thermo-mechanical detectors, bi-material THz sensor arrays take advantage of intrinsic material properties to deform when they absorb incoming radiation.

Bi-material sensors usually have regions with two layers of materials with a large difference in thermal expansion coefficients. As thermal energy increases

inside the sensor, the layer with the greater expansion coefficient expands more than the other one. Since both layers are connected, the difference in stress gradient across the element causes the cantilever to deform.

The challenge is to have the sensor temperature increase proportionally to the amount of incident THz radiation. One possible technique is to establish a distance between two material layers of the sensor with dimensions that characterize a resonant cavity inside the sensor [13]. The resonant cavity is the central part of each sensor. It has properties that allow it to combine incident waves at a specific frequency, reinforce the wave with an internal standing wave, and increase the energy inside the cavity. The dimensions of the cavity can tune the frequency of the illumination source, which provides improvements in energy absorption and temperature rise. The resonant cavity also serves as a reflector in the configurations employing the optical readout.

As important as having the maximum bending movement of the cantilever with internal temperature increase, is a fast recovery to the original position when the THz radiation diminishes or stops over the sensor surface. This property becomes important when using the array for real-time imaging, and to promote a fast return, two techniques of illumination can be used: transmission and reflection.

Both cited techniques aim to allow the sensor's perception of the contrast in THz intensity radiation between the object and the background. They can be described as follows:

- Transmission: The source of the THz is positioned in front of the sensor array and inside its FOV. All radiation that surrounds the object reaches the sensor with maximum intensity. The radiation that strikes the object is blocked or weakened by the object itself, generating a shadow over the sensor. The differences in energy along the array will form the image of the object, as illustrated in Figure 4.



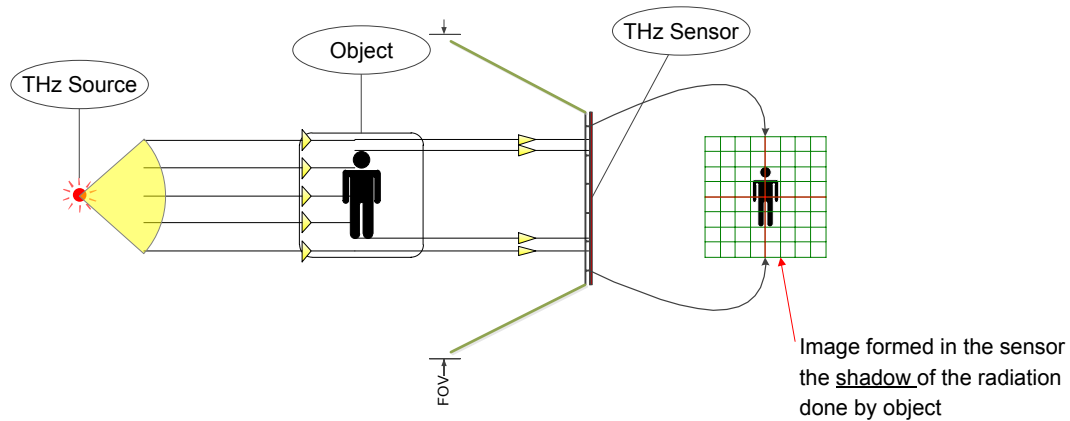


Figure 4. Schematics of the transmission illumination technique wherein an image is formed by the shadow of radiation.

- Reflection: The source is positioned on the same side of the object as the sensor and illuminates the object from an offset angle. The radiation that strikes the object is reflected with several intensities, depending on the material components of the object. The differences in energy along the array will form the image of the object, as illustrated in Figure 5.

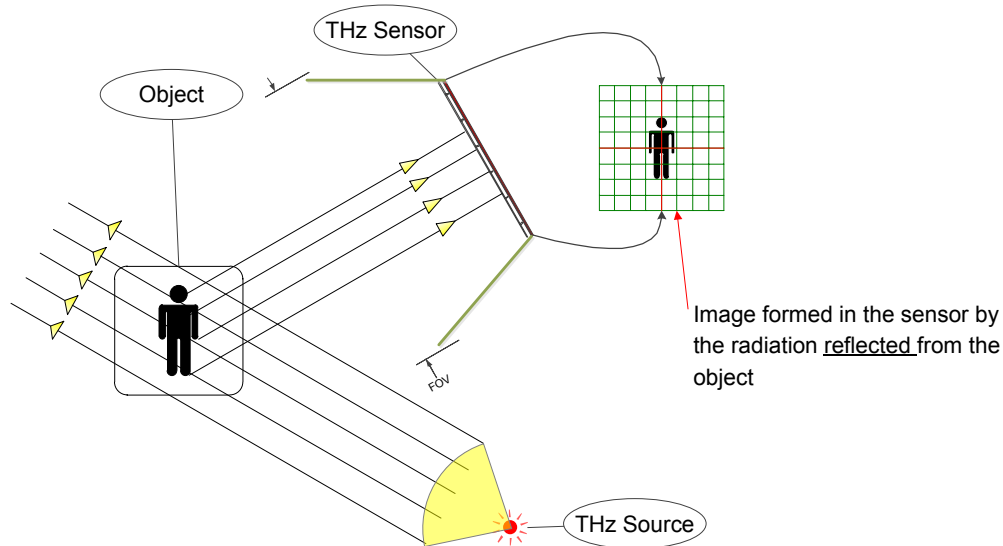


Figure 5. Schematics of the reflection illumination technique wherein an image is formed by the radiation reflected from the object.

The sensor operating parameters have a strong relationship to the MEMS design; therefore, the sensor's design has to be optimized to improve the performance in accordance with the application.

## B. SENSOR STRUCTURE

MEMS sensor arrays can be designed employing microcantilevers; several similar structures have been reported [10], [30], [32], [35].

Bi-material MEMS sensors are structures that react to radiation with structural deformation (bending). Figure 6 shows a section of a bi-material sensor array and details of an isolated sensor.

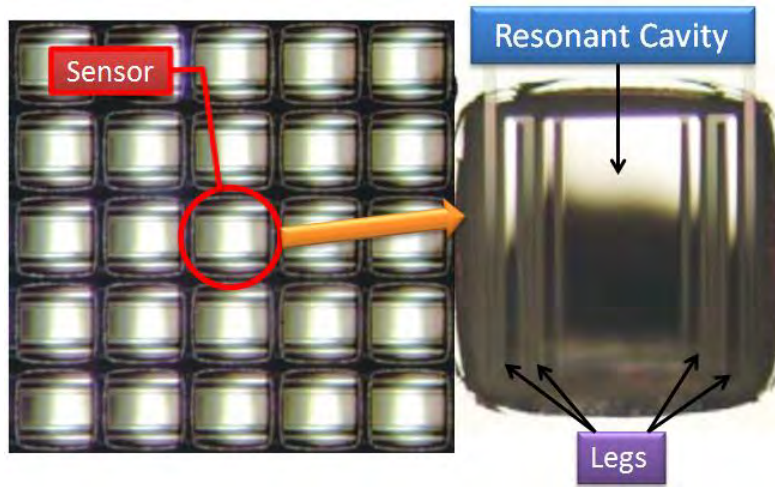


Figure 6. Part of a sensor array and an enlarged view of one isolated sensor with highlights on the regions of its structure. After [10]

Three regions comprise the sensor:

- The absorbing region designed to convert THz energy into heat (Resonant Cavity/Reflector);
- The bi-material elements that convert heat into mechanical bending (Legs); and
- The anchor that holds the sensor onto the substrate.

This sensor features a multifold bi-material structure described by Senesac et al. [36] and Guo et al. [37], and illustrated in Figure 6. The major advantage is maximizing the displacement due to the bimetallic effect under

increase in temperature, while preserving the compactness of the structure [13]. A pictorial representation of the sensor used in this work is shown in Figure 7.

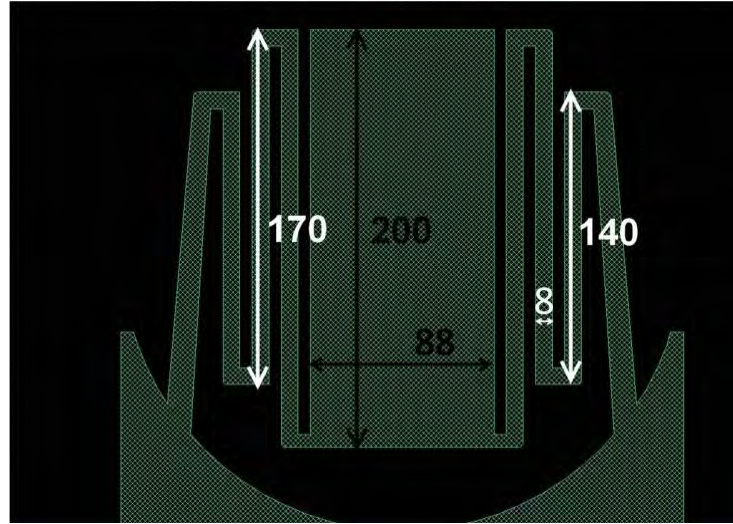


Figure 7. Bi-material sensor structure (dimensions in  $\mu\text{m}$ ). After [38]

In Figure 7, the central part represents the resonant cavity designed to absorb radiation energy in the range of frequency of interest as well as to reflect the probing illumination. The legs surrounding the central part are thin in order to provide thermal insulation of the resonant cavity as well as bi-material deformation under radiation illumination. The anchor pads assure the stability of the structure through the microfabrication process; they hold the sensor and, also very important, assure the necessary heat flux.

The dimensions, geometry, material intrinsic properties, and fabrication technique control the final properties of the sensor, such as sensitivity, speed of operation, and noise.

### C. SENSOR COMPONENTS

To achieve the necessary sensitivity to THz radiation the sensor is constructed using two materials: aluminum (Al) and silicon-dioxide ( $\text{SiO}_2$ ). The  $\text{SiO}_2$  is the basis of the structure. The Al is applied over four legs for bi-material effect, and over the resonant cavity for reflection purposes.

The application of these two materials is sufficient to obtain the bi-material thermo-mechanical bending movement, but a thinner film of silicon-nitrite ( $\text{SiN}_x$ ) has to be implemented between the two layers to create a resonant concavity that improves the conversion of THz radiation into thermal energy [13].

A schematic distribution of Al and  $\text{SiO}_2$  material over the pixel's structure is shown in Figure 8. The  $\text{SiN}_x$  (not shown) is sitting between those two layers. As described by Grbovic and Karunasiri [13], this material distribution design provides a good bending capacity to the pixel's structure.

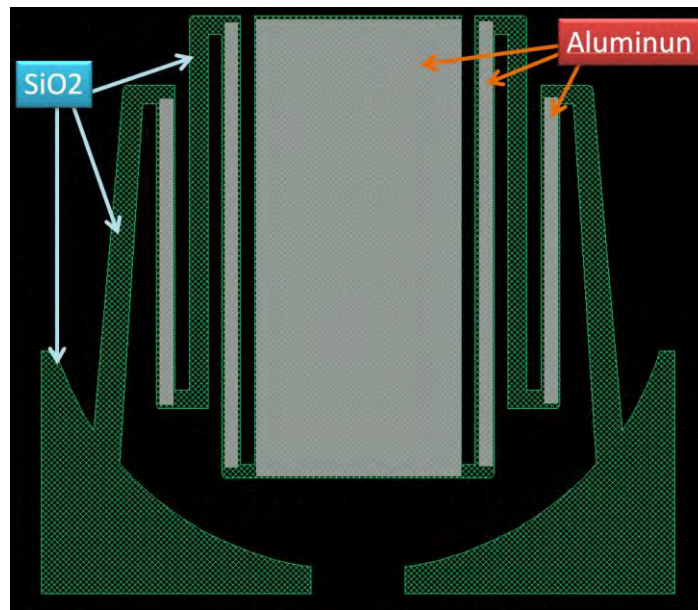


Figure 8. Material distribution over the pixel's structure. After [38]

The presented sensor architecture does not offer much value if the information generated by the dynamics of the thermo-mechanical structure, when illuminated by THz radiation, cannot be extracted and converted into data that can generate an image. Thus, advantage can be taken of the reflectiveness of the Al layer by designing an optical readout to measure the reflected visible light from the cantilever and then to infer the amount of THz radiation that is reaching the pixel. The following chapter contains a description of how that optical readout design works and how to extract information from a bi-material sensor using that technique.

## **D. OPTICAL READOUT FOR BI-MATERIAL SENSORS**

As explained in Chapter I, the research group of the NPS Sensor Research Laboratory chose the optical readout technique to be used in the THz imaging system using the MEMS bi-material sensor array due to its simplicity, low cost, and reliability.

### **1. Concept**

Optical readout can be understood as a process of information reception, conversion, and display from a device to a user in a readable format using optical resources. Its principle of operation for IR detection has been previously reported [39] and could be applied on the same basis for THz imaging using bi-material sensor arrays.

Two types of optical readout techniques can be cited as useful: [10]

- One-sensor probing; and,
- Multiple-sensor probing.

Both techniques use the reflection of light from a source to measure the deflections of the sensor's microcantilevers. The major difference between these two techniques is the size of the light beam used to probe. In the first technique, light from a laser is directed toward to a single sensor and is based on the approach developed for the atomic force microscopy (AFM). In the second, a wide beam probes all sensors in the array, allowing a simultaneous readout (Figure 9) [10].

In this work, multiple microcantilever probing was used since higher rates of frames per second (fps) can be achieved [33].

### **2. Multiple-Sensor-Probing Configuration**

In this configuration, a readout light source produces a beam that illuminates all surface areas of the sensor array. The light is then reflected by each sensor in the array and projected onto a CCD via a set of lenses, as illustrated in Figure 9.

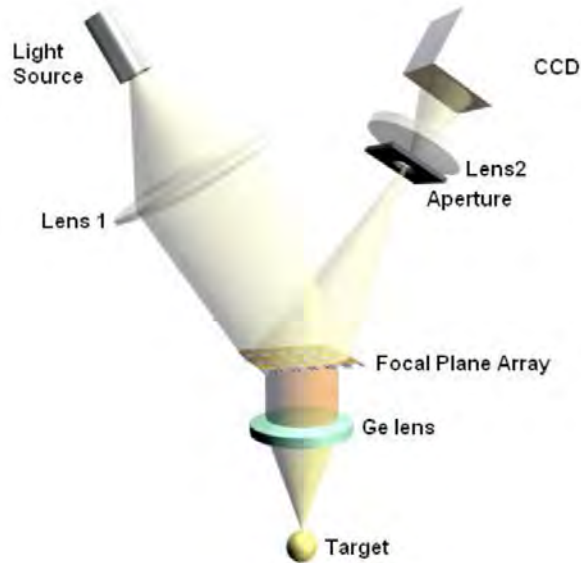


Figure 9. Schematic example of multiple-sensor probing using one light beam to illuminate all sensors in the array, and the reflections from all sensors captured by a CCD camera simultaneously. From [10]

In Figure 9, at the opposite side of the optical readout, a THz source illumination for use with the transmission technique, as was explained in topic B, can be observed.

The key component of this configuration, that makes the CCD sensitive to the sensors' bending variations, is the aperture (Figure 9). The aperture should be positioned on the spectrum plane generated by a Fourier lens. The principle was demonstrated by Zhang et al. [40] using a knife-edge filter operation (KEFO), which is effective but demands a uniform bending behavior from all sensors of the array. A circular aperture does the same function as the knife-edge filter but acts as a filter for any bending direction of the sensors.

At the spectrum plane, there is the diffraction spectrum of all array reflection at the same time. If any sensor bends, it will change the position of the higher-intensity spot of the beam at the spectrum plane and will be blocked since it goes out of the aperture.

Therefore, the diameter of the aperture, in conjunction with other features of the readout, will determine the sensitivity of the resolution to sensor bending. The smaller the aperture, the better the resolution of the readout; but this reduction in size is limited by the sensitivity of the CCD, the wavelength of the light used, and the power of the light source used in the readout.

Another natural aspect, important in determining the sensitivity of the resolution to sensor bending, is the distance of the sensor array from the CCD. This is a geometrical issue in which the farther the sensor is from the CCD, the greater the changes in position of the light beam reflected by the sensor toward the CCD. Thus, changes in intensity can be captured by the CCD with fewer degrees of sensor bending. This distance is limited by the illumination capacity of the light source inside the readout and by the optical properties of the set of lenses.

To obtain images in this configuration, the system in a starting-point position has to be aligned. Starting with the sensors at minimum displacement, the entire array has to be rotated in order to provide maximum reflection toward the CCD camera. At that point, the camera can generate an image of several bright spots that are associated with each pixel of the sensor. Then, the system is aligned and that first image has to be recorded as a reference background. After that, any movement in the sensors can be interpreted by comparison between actual CCD images and the recorded reference background.

This readout technique of probing multiple detectors simultaneously has the advantage of higher fps rates, but there are limitations to be considered in extracting information from the MEMS sensor arrays.

### **3. Optical Readout Limitations**

Noise is an important limitation in imaging systems. Aspects such as temperature fluctuation-limited and background-limited noise are applicable to all THz sensors [10] and can affect the readout performance. The major noise

sources for bi-material sensors are the thermo-mechanical noise from the microcantilever's thermally excited vibration, and shot noise from the optical readout system [33].

The fundamental performance limitation of a bi-material sensor array comes from its intrinsic noise property. An ideal, noiseless readout amplifies both the useful signal and the detector's intrinsic noise without distorting them or changing the signal-to-noise ratio (SNR). In fact, there is no practical ideal, noiseless readout method; and, in the best case, the inherent SNR of the sensor can be decreased only minimally [10]. Noise effects on the final image are difficult to eliminate but can be diminished by image post-processing software techniques.

Taking into account all limitations, and encouraged by the set of potential benefits of the optical readout for the MEMS sensor array, an optical readout setup for probing multiple detectors was designed and assembled. It is described in the following chapter.



### III. DESIGN AND ASSEMBLY OF OPTICAL READOUT SIMULTANEOUSLY PROBING MULTIPLE DETECTORS

#### A. GENERAL DESCRIPTION

In order to achieve a compact configuration and give a better control of the illumination angle offset, a design that follows the principle illustrated in Figure 9 was used, but with a different distribution of the components. The optical readout architecture used in this work is schematically illustrated in Figure 10.

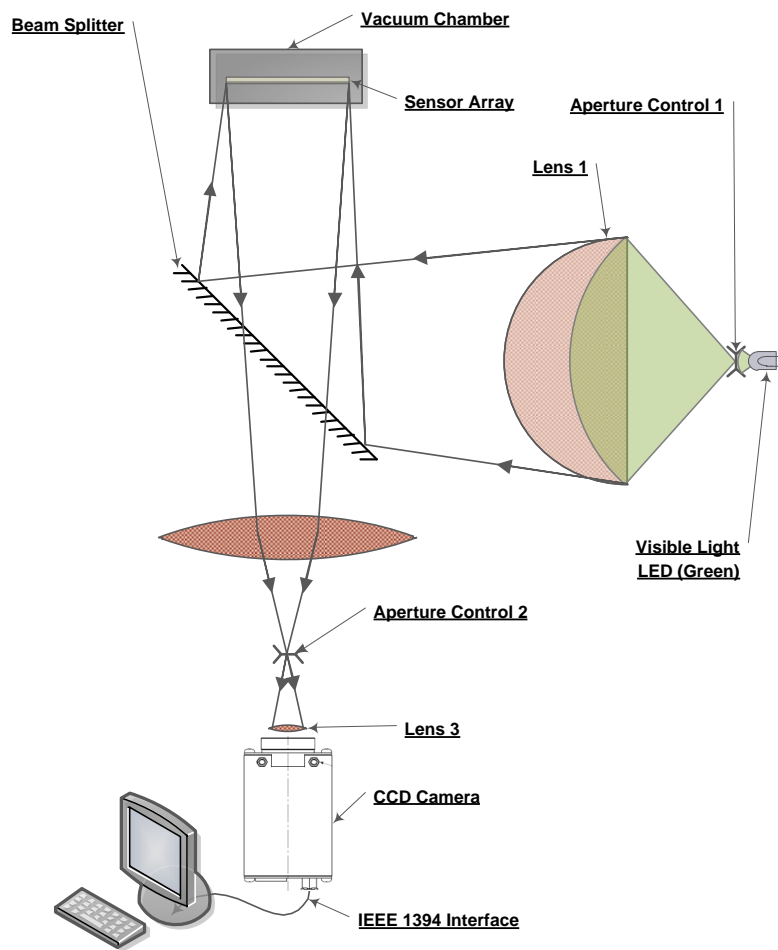


Figure 10. Architectural design for optical readout for probing multiple detectors.

The visible light that comes from the green LED through aperture 1 becomes convergent via lens 1, which is used as the beam convergence angle controller. Subsequently, the light is directed by a beam splitter to the sensor that reflects the beam back to the beam splitter and then, via lens 2, aperture 2, and lens 3 to the CCD camera (Figure 10). The camera is connected to a computer via a link FireWire (IEEE 1394); and a software application, developed in LabView [41], controls all camera operation and image processing.

The displacement of all sensors is simultaneously measured and projected as a spatially-varying visible light image onto the CCD camera. Each pixel on the sensor reflects a small portion of the readout light, directly related to its position. When deformation occurs, the direction of the reflected beam changes. To avoid cross-talk between pixels, aperture 2 works as a spatial filter that limits the radiation to the CCD, as explained in Chapter II. The individual sensors are mapped into the CCD via direct transformation; therefore, a fixed area on the CCD is imaging its corresponding sensor.

In Figure 11, a generic diagram illustrates the aperture working as a spatial filter blocking the reflected rays coming from a deflected sensor.

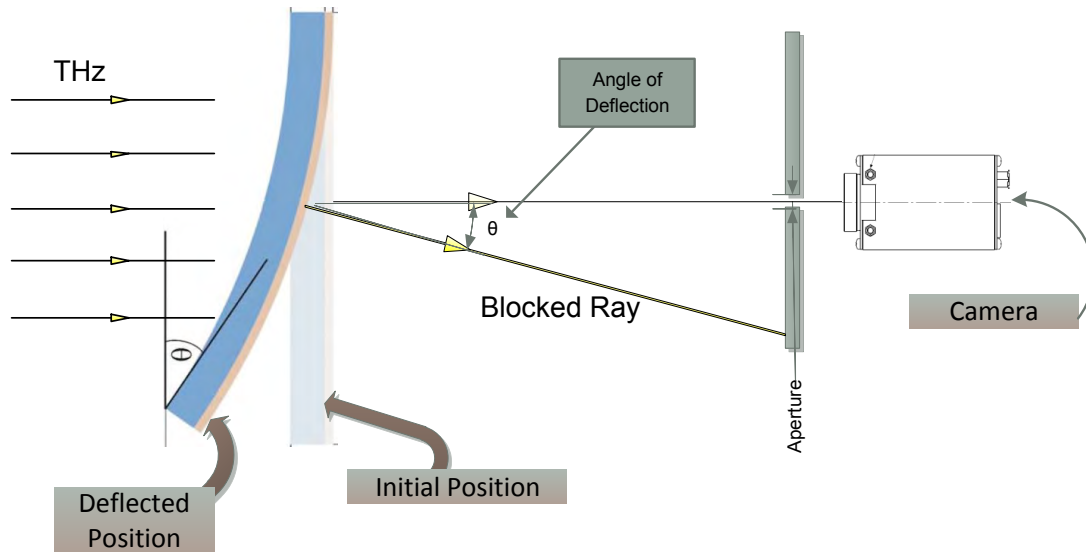


Figure 11. Diagram showing aperture blocking reflected rays coming from deflected sensor.

To reduce imperfections in the sensor array and background deformations, the software application needs to obtain a steady image of the sensor array without THz illumination, when all of the detectors are in their equilibrium position. This first image is used as background to be subtracted from all subsequent frames. This technique permits a display of an image that contains the information only from sensors that change their positions.

To optimize the readout performance, bounded by availability, the readout components were selected as discussed in the following section.

## **B. READOUT SUBSYSTEMS**

### **1. Light Source**

The light source needs to generate a strong enough beam of light so that it can be reflected from the sensor and pass through all lenses and apertures, and still remain powerful enough to be detected by the CCD pixels. For a source with high power emitting at the optimal frequency of the CCD, a green-colored laser/LED was chosen.

Based on the CCD specifications, the LED XPEGRN-L1-0000-00A01 (Figure 12) was selected. It has a dominant-wavelength emission range from 520 nm (min) to 535 nm (max) [42].



Figure 12. Cree XLamp XP-E LED Green: used as the visible light source for the readout. From [43]

The LED employed emits 87.4 lm (Luminous Flux @ 350 mA) in a viewing angle of 130 degrees [43]. To contain the LED beam, an aperture control is placed in front of the source. Lens 1 controls the beam convergence before it reaches the beam splitter. The light source subsystem is schematically shown in Figure 13, and pictured in Figure 14.

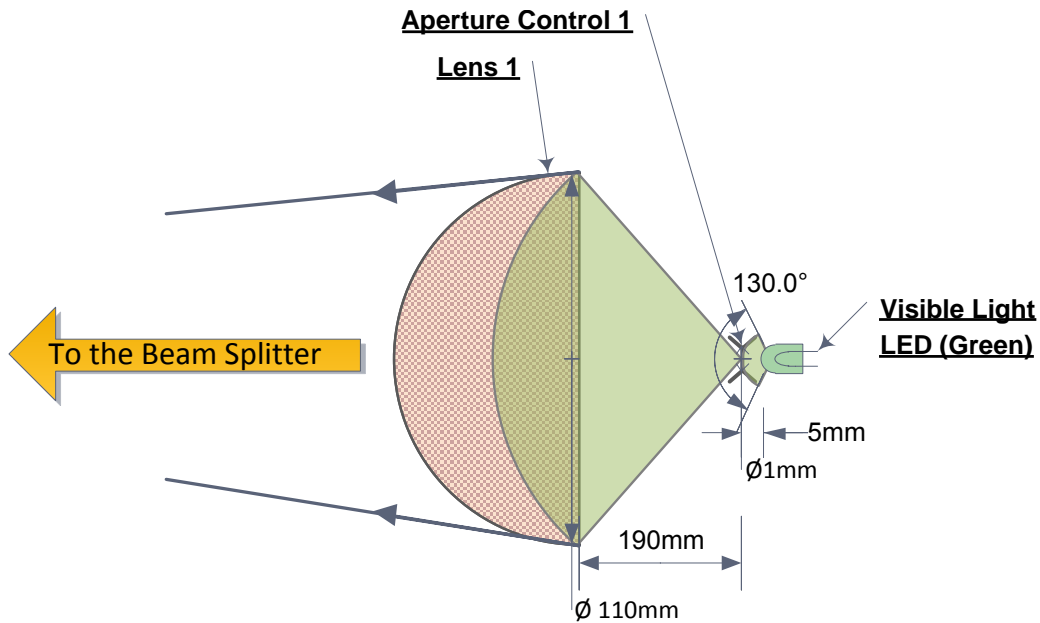


Figure 13. Light source subsystem scheme shows how the beam emitted by the LED is controlled by the aperture in order to illuminate the complete area of the Lens 1.

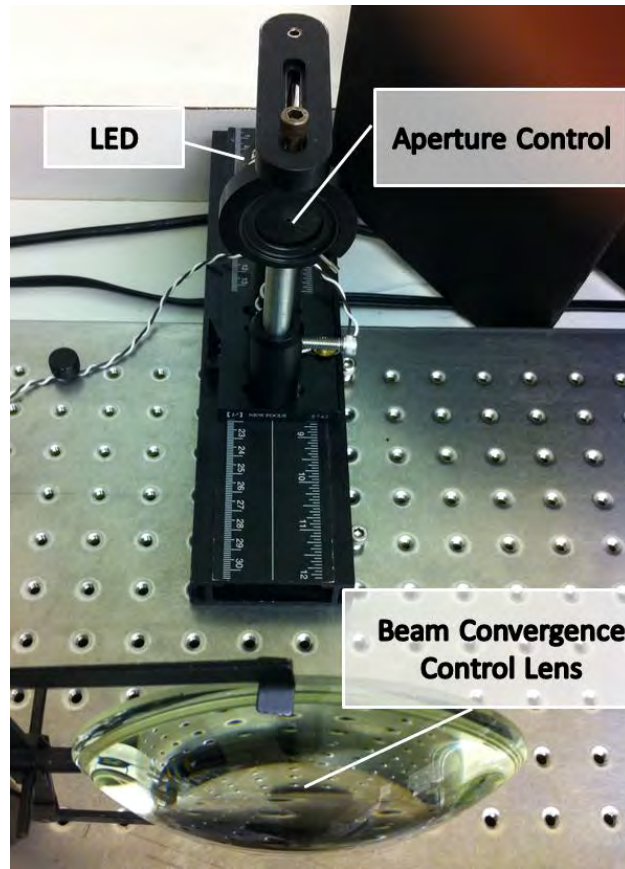


Figure 14. Light source subsystem photo showing the components assembled in the laboratory.

In Figure 14, the LED and the aperture control can be observed placed on an optical rail, which permits distance adjustments to the lens and, consequently, the beam convergence to the beam splitter.

The lens for beam convergence control is 110 mm in diameter with a focal length of 150 mm. This size is necessary to produce a beam convergence that can illuminate all areas of the sensor's array. A collimated beam was not used for the following reasons:

- Magnifying the image of the sensor using all the area of lens 2 is not desired; otherwise, too many distortions are obtained on the image plane; and,
- Using convergent beam lens 2 can be employed with a longer focal length, which produces less distortion to the image and maintains the compactness of the setup.

The distance from the LED to the aperture control is established visually, so the LED has to be placed at a distance from the aperture control great enough to produce a beam that covers the entire area of lens1.

This distance from the aperture to lens 1 has to be greater than its focal length; thus, a convergent beam is produced by this lens. The convergence of the outward beam from lens 1 is also controlled by this distance, and a convergence is established in order to produce a beam that illuminates the complete area of the sensor array. Another parameter that has to be observed when adjusting this distance is the position of the spectrum plane that has to be placed after lens 2, as described in the next section.

## **2. Lenses and Aperture Control**

From the light source subsystem, the convergent beam is directed to the sensor by a beam splitter (Figure 10). Light coming from the sensor passes through the beam splitter, and all rays are converged by lens 2 to the aperture at the spectrum plane. The rays coming from aperture 2 are captured by lens 3, which allows an image to be formed at the camera's CCD. A schematic illustration is shown in Figure 15.

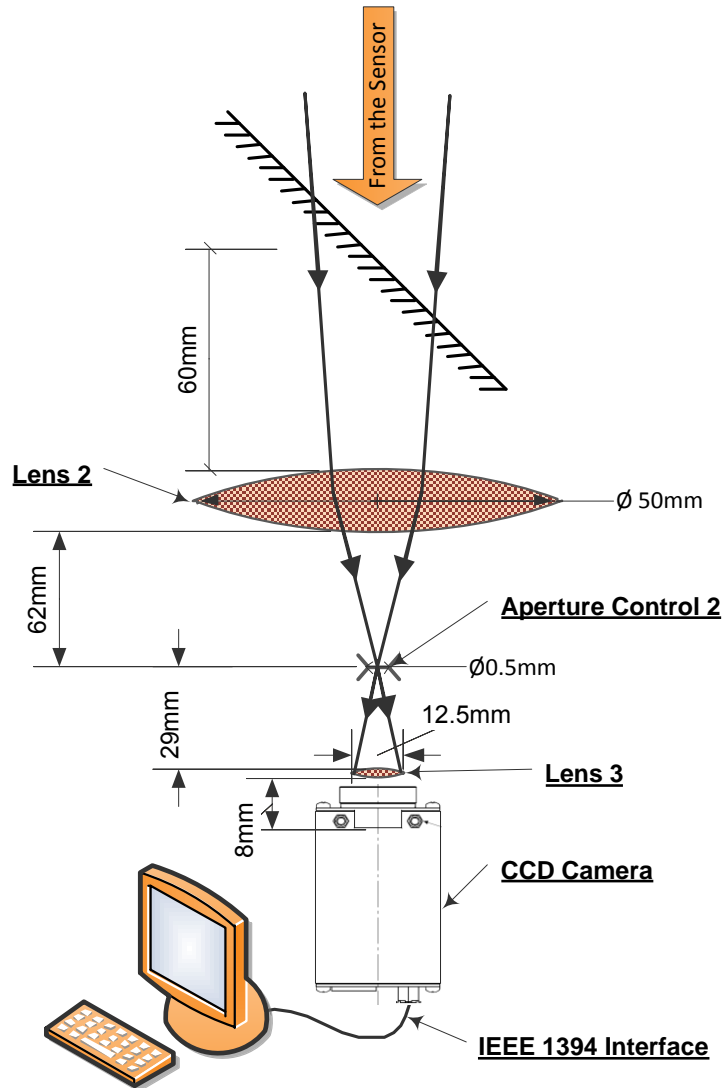


Figure 15. Lenses and aperture control sub-system showing Lens 2 controlling the convergence of the beam to Aperture Control 2, and Lens 3 forming image into the CCD.

Lens 2 has a 50-mm diameter and a focal length of 100 mm. Aperture Control 2 sets the aperture diameter to 0.5 mm, and Lens 3 has a 12.5 mm-diameter with a focal distance of 37 mm. All components are pictured in Figure 16 as they were assembled in the laboratory.

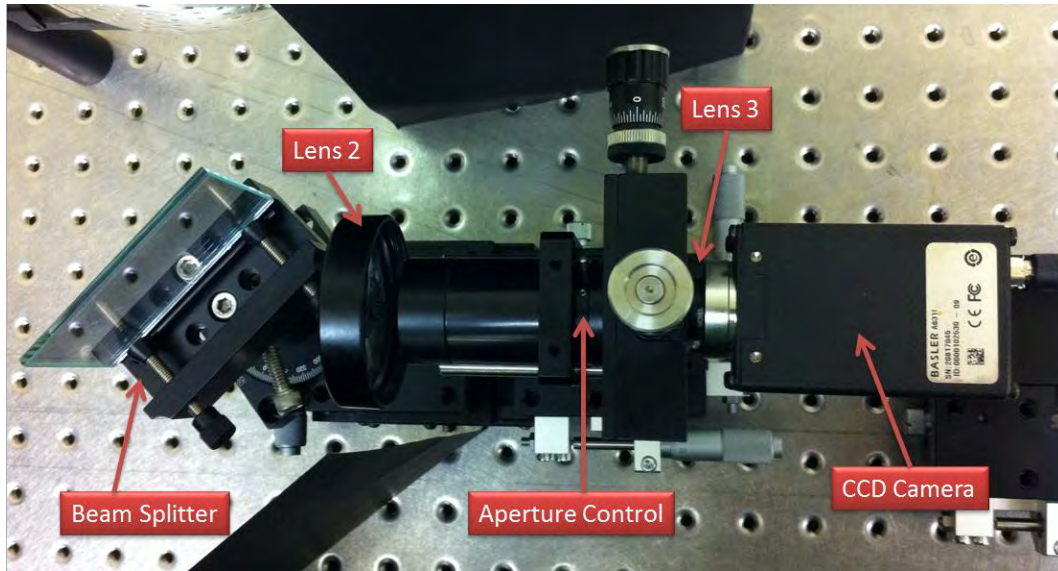


Figure 16. Top-view picture of the lenses and aperture control subsystem assembled in laboratory.

It may not be clear in Figure 16, but all components are mounted on mobile bases to permit alignment and necessary distance adjustments between the components.

To align this subsystem, a mirror was used in place of the sensor with the light source turned on. The first component to be aligned was the beam splitter in order to reflect the light source with an angle of 90 degrees, as shown in Figure 10. Subsequently, Lens 2 was placed with the beam passing through the center of the lens. Then Aperture 2 was aligned at a distance that allows the higher density of the spectrum to remain at the center of the aperture. To place the camera in the proper position, the mirror was replaced with the sensor array again, and Aperture 2 was left in the open position. Observing the image captured by the camera on the computer, Lens 3 and the camera were positioned in order to have a focused image, with the sensor array covering almost all the area of the image.

The main function of lens 2 is to control the convergence of the beam to Aperture 2. The beam passing through a small part of this lens is allowed just to



avoid distortion at its borders. In this readout, the lens could be used with a long focal length (100 mm) to maintain the compactness of the setup because of the convergence of the beam from the source, as explained in Chapter III, Section B-1.

The size of the sensor array in the image is important to permit a maximum number of pixels representing one sensor. In our case, the readout allowed us to represent each sensor by an area of 8 x 8 pixels on the image. The size of the area representing each pixel is related to the size of the sensor array and the size of the CCD; thus, there are no adjustments that could increase this area if the objective is to image all sensors in the array. Having a small area of the sensor represented on the CCD is bad for the imaging process because the noise at the camera would be more prominent, confusing the image.

Next, Aperture 2 can be closed to the minimum aperture size (0.5 mm) and the generated image checked. At this moment, gain and shutter speed of the camera have to be adjusted to those light conditions. The aperture can also have a fine adjustment in order not to allow blocking the visualization of any part of the sensor array.

Finally, this subsystem is ready to be used to align the sensor array under THz illumination, and then to run the imaging of an object.

### **3. Sensor Vacuum Chamber**

To hold the sensor array, a vacuum chamber was fabricated at NPS Physics Department. Low pressure environment reduces the heat exchange between the sensor and the surrounding air as well as the vibrations caused by air pressure fluctuations. One side of the vacuum chamber has a Tsurupica window, which is almost completely transparent to THz radiation. On the other side, the chamber has a quartz window transparent in the visible readout light.

The Tsurupica window has a good transmission performance in the THz range, mainly between around 1 THz and 7 THz, as shown in Figure 17. That

range is adequate for the range of quantum cascade lasers to be used in this imaging system. The graph in Figure 17 was obtained by Microtech Instruments, Inc. [44]. To check the performance of the Tsurupica window used in the vacuum chamber, measurements were made with the FTIR Spectrometer of the Sensor Research Lab, and the same performance results were obtained.

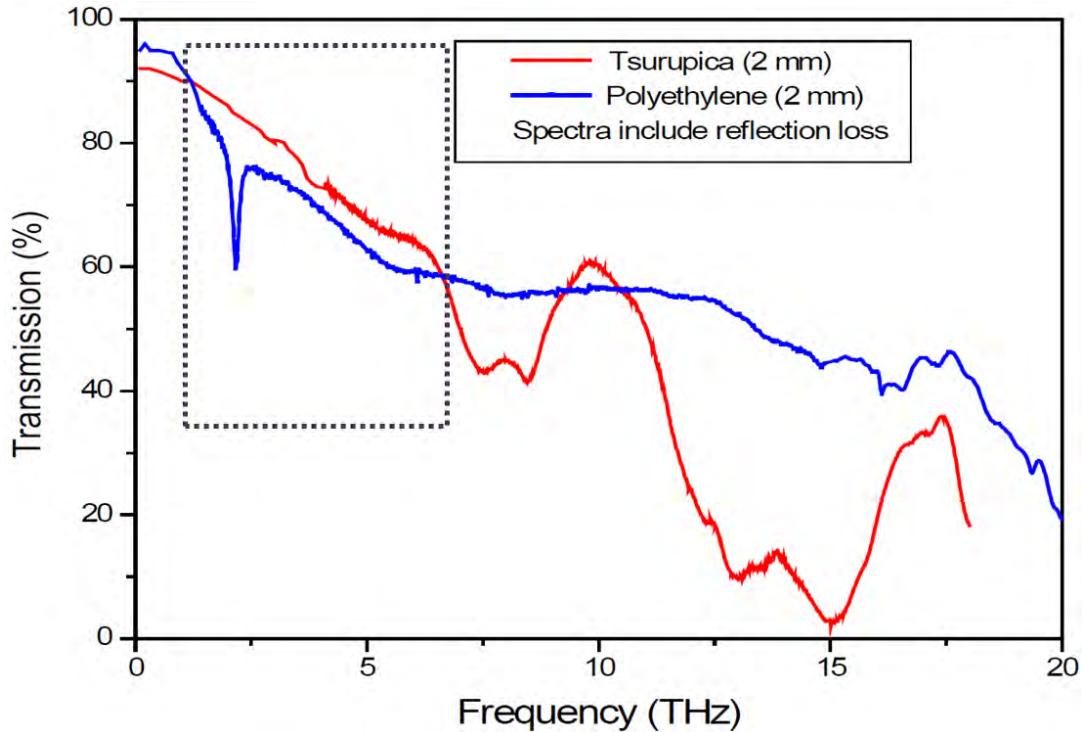


Figure 17. Transmission spectra of tsurupica and polyethylene in THz spectral range with the area of interest for this work highlighted. After [44]

In Figure 18, the vacuum chamber on a rotating mount can be seen from the window for the visible range side. That window is seated on the chamber's hole in an inclined position to avoid undesired reflection toward the CCD camera. The rotating mount would be necessary for the initial alignment of the array to an adequate angle of reflection, as explained in Section A of this chapter.

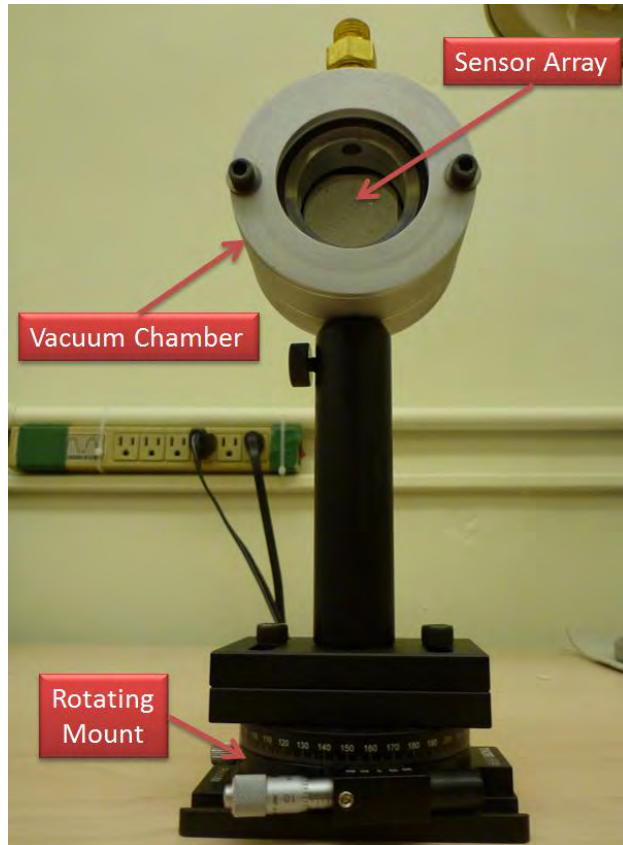


Figure 18. Picture of the vacuum chamber on a rotating mount from the window for the visual range side. The sensor array can be observed inside the chamber.

This vacuum chamber was not used in the readout setup during the alignment test and readout characterization because it was not necessary for that purpose, but it will be necessary for the integration of the readout setup with the THz imaging system.

#### 4. CCD Camera

The Basler A631f–CCD Camera used in the readout is a monochrome area scan camera that employs a CCD sensor chip. The sensor chip provides a full-frame shutter, an electronic exposure time control, and other control features and is programmable via IEEE 1394 bus [45].

The major components of the camera are a CCD sensor, one Variable Gain Control (VGC), and one Analog to Digital Converter (ADC). The pixels in the CCD sensor output voltage signals when they are exposed to light. These output signals are amplified by the VGC and transferred to the ADC, which converts the voltages to digital output signals. The camera has digital output signals represented by 12 bits or 8 bits [45].

For our application, the camera output mode was set to 8 bits per pixel; thus, black pixels on the output image should have a gray value of 0 and white should have a gray value of 254, for a total of 255 gray-value levels. Work with the camera output of 8 bits was selected because it presents a smoother image in the presence of noise than the 12-bit mode, which has more gray-value levels and is more sensitive to noise.

The CCD used in the camera is a Sony ICX267AL. It is a diagonal 8 mm (Type1/2) interline CCD solid-state image sensor with a square pixel array and 1.45 M (1392 (H) x 1040 (V)) effective pixels. It works with a progressive scan, which allows all pixels' signals to be output independently in non-interlace format in 15 fps. All pixels' signals within the same exposure period are read out simultaneously, making this mode suitable for high resolution image capturing. The pixel size is 4.65  $\mu\text{m}$  (H) x 4.65  $\mu\text{m}$  (V) and the substrate material is silicon [46].

The wavelength of the light source was chosen based on the spectral sensitivity of the CCD that has its maximum quantum efficiency around 44% between 500 nm and 525 nm [47] as shown in Figure 19, which corresponds to green-color light.

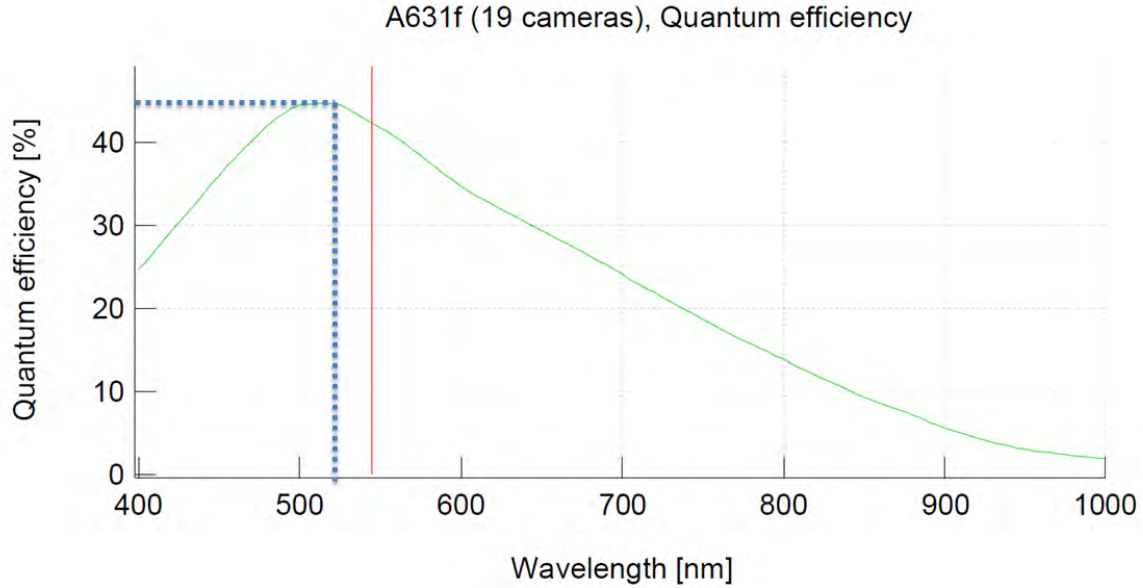


Figure 19. Graph of quantum efficiency for CCD camera Basler A631f with the maximum quantum efficiency highlighted (dashed blue) at around 525nm of wavelength. After [47]

### C. CAMERA SOFTWARE CONTROL

A software application was developed since the CCD camera for the optical readout setup has to acquire the image of the sensor and additional tools are necessary to help the user observe and analyze the sensor pixels' movement dynamics. To build the application, the Labview 2010 64-bits was employed [41].

Labview is a graphical programming environment from National Instruments, Inc., used by engineers and scientists to develop sophisticated measurement, test, and control systems using intuitive graphical icons and wires that resemble a flowchart. It offers integration with various hardware devices and provides built-in libraries for advanced analysis and data visualization [48].

#### 1. General Design

The objective of the application is to permit the operator to configure the camera depending on the environment or imaging needs. After that, the application should first acquire an image as a background frame, then continuously acquire current image frames, subtracting the background from

each subsequent frame. The operator can observe the modifications in the imaged object from a display and from a pixel histogram. Tools are available to modify the image presentation and the histogram graphs “on the fly.” If necessary, the operator could selected a specific area of the image and obtain statistical values (mean, minimum, and maximum intensities, and standard deviation) from the selected area. The application also should display the edges of an image where only pixels within a designated range of grayscale values appear to the user. The user can specify different methods and select what type of edge-detection filter is more adequate to an imaging circumstance. Figure 20 represents all functions of application.

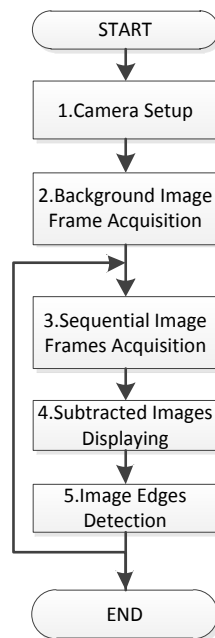


Figure 20. High-level application flowchart.

#### **a. Camera Setup**

The camera needs to be set before starting the application and initiating the acquisition. An overview of this process is shown in Appendix A, Figure 38. First, the camera ID that should be connected to the computer via an IEEE 1394 interface has to be selected. Then the desired shutter and gain value

have to be adjusted. In our setup, since work with a very small aperture is needed, the maximum values for these parameters have been chosen:

- Shutter: Was set to 4095 which represents 81.9 ms exposure time and thus permits a maximum frame rate of 12 fps [45];
- Gain: With a gain of 0 dB, a gray value of 1 is produced when the pixels are exposed to no light and a gray value of 255 is produced when the pixels are exposed to bright light. 0 dB of gain is achieved when the value was set to 350. In the setup, the gain was set to 1023, which is the maximum possible value for the camera and represents a gain of 25.9 dB [45].

All selected configuration and all camera setup information are presented to user on the human-machine interface (HMI).

#### ***b. Background Image Frame Acquisition***

It is necessary to subtract background information from the current image since the readout objective is to take differential displacement information from each pixel of the sensor, no matter what its initial or final displacement position was. To obtain the background, a buffer delay was set so that the process can wait for the camera stabilization before one frame is recorded. For the camera used in the setup, a delay of 10 units works fine. It means that the software just records one frame after 10 frames have already been acquired. This is the first process, and no other process runs before the background is recorded. The acquisition is done based on camera setup information, displayed to the user and recorded in the computer following a designated file path in BMP format. This process is schematically represented in Appendix A, Figure 39.

#### ***c. Sequential Image Frame Acquisition***

The objective of this process is to get current image information from the sensor. It starts after the background image has already been acquired and is similar to the background acquisition process but runs in a loop sequence that can be stopped only by the user action. Additionally, this process shows the

user a histogram of all pixel values for each captured image frame. All captured frames are recorded in the computer, following a designated file path in AVI format. This process is schematically represented in Appendix A, Figure 40.

#### ***d. Subtracted Image Display***

Image subtraction is the most important process of the software application. This process permits the user to visualize only the information of sensor displacement, thus observing the target object's shape from the sensor. A similar technique to obtain a THz image was reported by Yasuda et al. [49] in a nondestructive measurement of opaque material in a visible range. There are two types of subtraction in this process:

- Simple: Pixels with the same coordinates have their current values subtracted from the background ones. If the subtraction results in negative value, the pixel is displayed in minimum value that is black.
- Absolute: Pixels with the same coordinates have their current values subtracted from the background ones. Only absolute values result from this operation, and the pixel is displayed in an equivalent gray value.

Both results from subtraction are stored in the computer in separate AVI format files. In real time, the results are displayed to the user as images and as pixel–value histograms.

To obtain numerical values from a specific area of the image, the user can select an area by giving its coordinates. Then, the selected area is highlighted on the image's displays, numerical statistics (mean intensity, standard deviation, minimum intensity, and maximum intensity) are shown, and a corresponding histogram is displayed at the same time. A schematic representation is shown in Appendix A, Figure 41.

#### ***e. Image Edge Detection***

In the edge detection process, edges along a line of pixels in the image in the display can be found. This function can be used to identify and locate discontinuities in pixel intensities of an image that are associated with big



changes in pixel intensity values. Big changes in intensity values characterize the boundaries of the object being imaged by the sensor.

Some spatial filters are available to the user for choosing the method to detect the edges in the image. The types of spatial filters available in the application are described in Table 1.

Table 1. Spatial filters available in the application. After [50]

<b>Filter Option</b>	<b>Description</b>
<b>Differentiation</b>	Nonlinear highpass filter that produces continuous contours by highlighting each pixel where an intensity variation occurs between itself and its three upper-left neighbors.
<b>Gradient</b>	Linear highpass filter that replaces each pixel by a weighted sum of its neighbors. The matrix defining the neighborhood of the pixel also specifies the weight assigned to each neighbor. It highlights the variations of light intensity along a specific direction, which has the effect of outlining edges and revealing texture.
<b>Prewitt</b>	Nonlinear highpass filter that extracts the outer contours of objects. It highlights significant variations of the light intensity along the vertical and horizontal axes.
<b>Roberts</b>	Nonlinear highpass filter outlines the contours that highlight pixels where an intensity variation occurs along the diagonal axes.
<b>Sigma</b>	Nonlinear highpass filter that outlines contours and details by setting pixels to the mean values found in their neighborhood if their deviation from this value is not significant.
<b>Sobel</b>	Nonlinear highpass filter that extracts the outer contours of objects. It highlights significant variations of the light intensity along the vertical and horizontal axes. As opposed to the Prewitt filter, the Sobel filter assigns a higher weight to the horizontal and vertical neighbors of the central pixel

To run this process, the user has to specify the range of the pixel's gray value that will be replaced by a specific one, also determined by the user. All pixels with values inside the specified range will appear in the display with the replacement value, that is, with the same gray value. All other pixels, those that are out of this range, will be displayed as black. Edge detection will run based on the selected spatial filter as detailed above. Final results of the process will be shown in separate displays. A schematic representation of this process is shown in Appendix A, Figure 42.

## 2. Front Panel

A unique interface was developed to control the camera and display all information to the user. A view of the entire front panel can be seen in Appendix B, Figure 43.

Before running the application, the user should specify the camera setup (Figure 21) and the file path setup using their respective HMI's. For the optical readout setup, the camera was set as described in Table 2, and the file path can be chosen freely by the user.

Table 2. Camera setup used in the readout.

Field Name	Value	Note
Session In	Img0	Define the name/address of the camera in the computer
Image Type	Grayscale (U8)	Define the image type and the number of grayscale levels in 255 (8-bits)
Background Buffer	10	Represents the number of frames that should be acquired before the background image is recorded.
Video Modes	33	Represent the output formats of the camera. In our case, number 33 represents <i>Format 7, Mode0, 1392x1040</i> .
Shutter	4095	Define the exposure time for the camera. The input value represents the interval of the time the shutter will remain open. This interval is computed by multiplying the input value times 20 $\mu$ s, which is the size of a standard slot.[45]
Gain	1023	It is the gain the received signal from the CCD will have at the ADC. The value 350 represents 0dB and 1023 represents 29.5 dB of gain. [45]

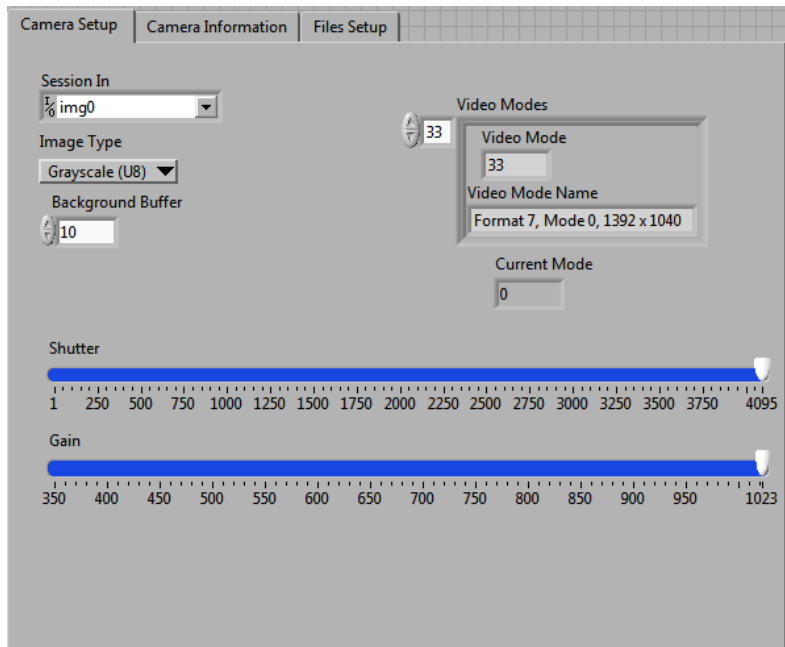


Figure 21. Camera setup HMI.

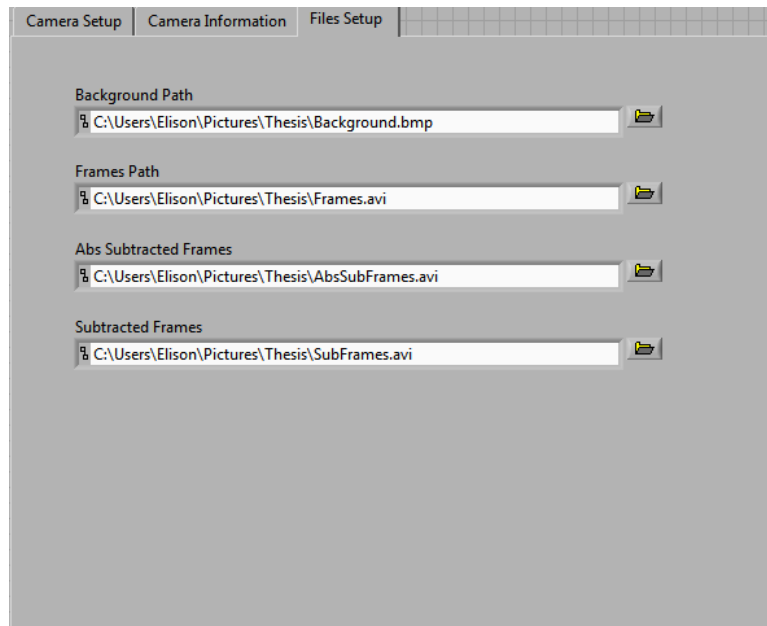


Figure 22. Files setup HMI.

After starting the application, the first image displayed to the user is the background and then the actual image. The actual image will continue to be updated, as will the actual image histogram, until the user stops the application. This information can be seen at the top part of the Front Panel shown in Figure 23.

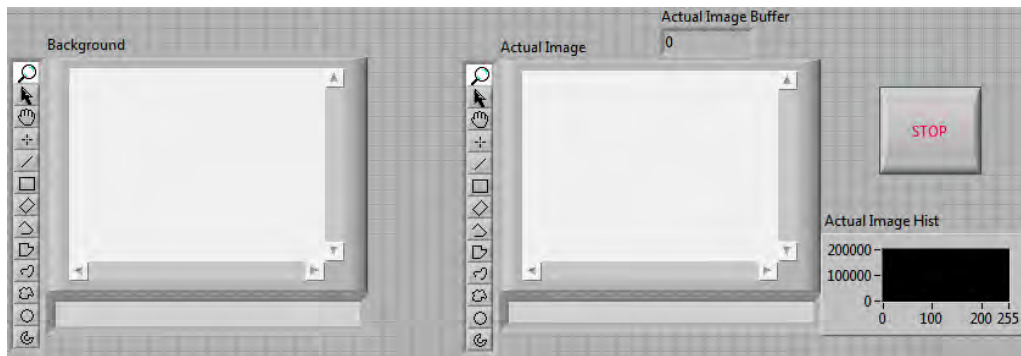


Figure 23. Background and actual image information displays.

The subtraction process results can be seen in two displays and two histograms on the Front Panel as shown in Figure 24.

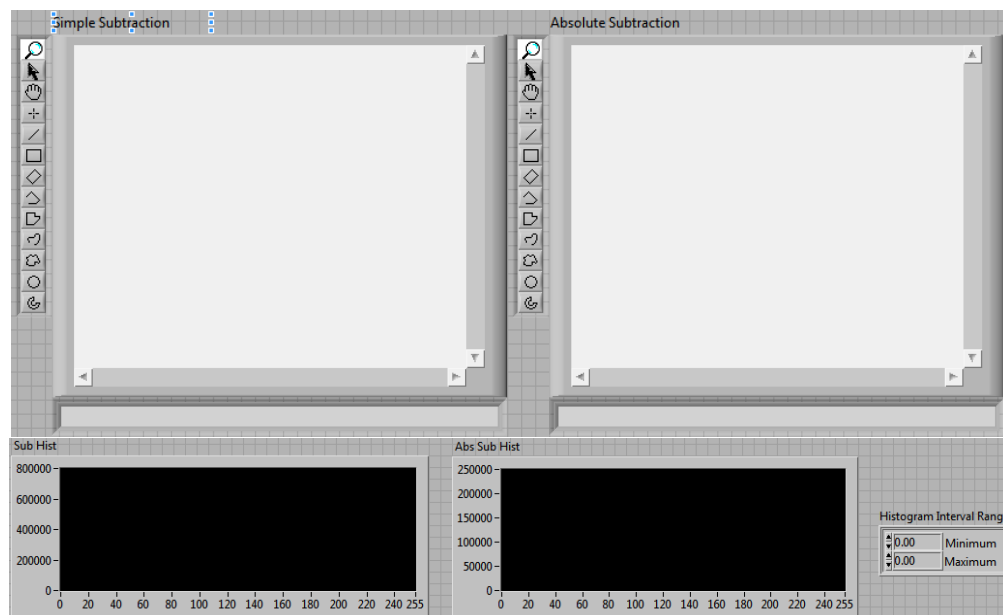


Figure 24. Simple and absolute subtraction images displays and histograms.

If desired, the user can obtain statistical information from a specific area of the subtracted images. To do that, the user has to specify the coordinates of the desired area using the *Rectangle Abs Subtraction Control* HMI on the Front Panel as shown in Figure 25.

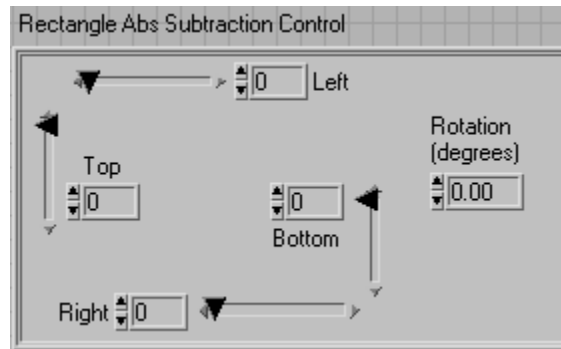


Figure 25. Image area selection control HMI.

After selection, the defined area will be highlighted by a rectangle over the image display, and all data from the area will be shown in a histogram and in the box *Gray Level Intensities–Abs Subtraction*. All tools used for area selection and display analysis in the Front Panel are shown in Figure 26.

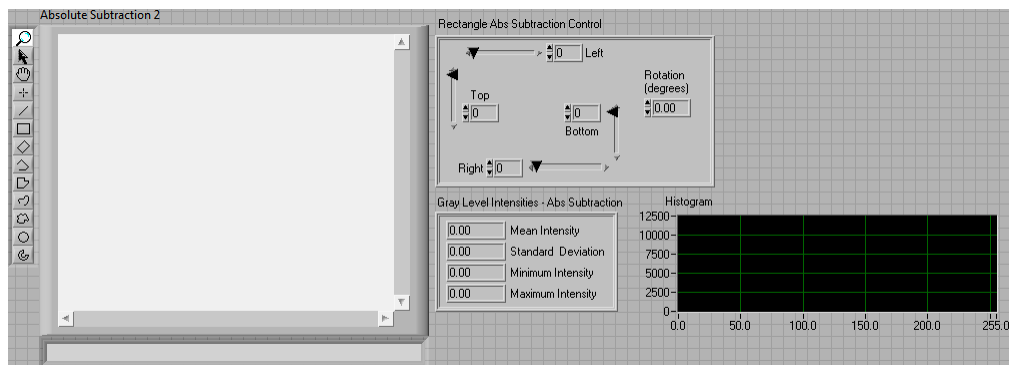


Figure 26. Area selection and display analysis tools HMI.

To configure and obtain the images from the Image Edge Detection process, the user has to select the desired filter for each image in fields *Edge Method* and *Edge Method 2*, and then establish the range of pixel values to be

replaced by a desired value. The results of this process will be displayed on the Front Panel. All these configuration tools and displays for edge detection are shown in Figure 27.

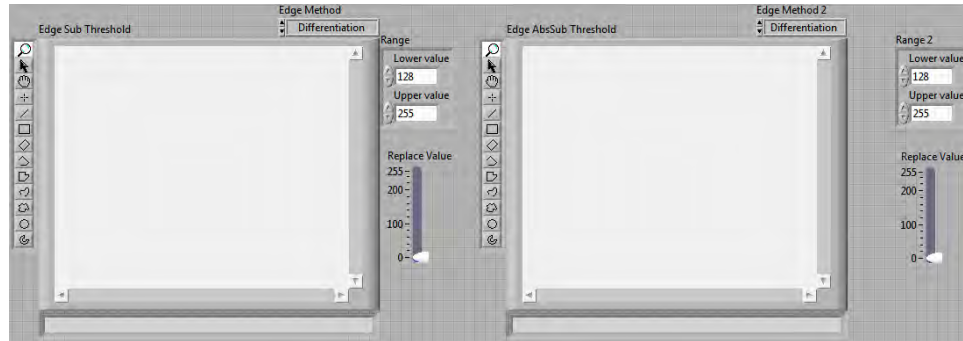


Figure 27. Image edge detection tools and displays HMI.

The Front Panel was configured using the LabView GUI tools. All objects used in the Front Panel have functionalities and connections. To set them, we had to use another GUI that works with blocks in a configurable diagram.

### 3. Block Diagram

After building the Front Panel, code using graphical representations of functions to control the Front Panel objects was added. The Block Diagram contains a graphical source code, and the Front Panel objects appear as terminals on the Block Diagram. The Block Diagram contains Terminals, Nodes, Wires, and Structures that permit the programmer to configure the source code as desired.

For this project, the block diagram was divided into sub-blocks that execute all implemented functions in a sequential way. All sub-block functions are described in Table 3 and a graphical overview of the block diagram is shown in Appendix C.

Table 3. Software application block diagram summary description.

Block	Summary Function Description	Schematic Representation (Appendix C)
1 <sup>st</sup>	Select one camera connected to the computer, define desired attributes, and initiate the camera to acquire the background image	Figure 44
2 <sup>nd</sup>	Execute the background image acquisition after the buffer delay, create and save a .BMP format file in a pre-selected file path. Display the image to the user. Stop the camera acquisition.	Figure 45
3 <sup>rd</sup>	Prepare the application to acquire the sequence of image frames, thus allocate memory to save all information in .AVI format files in a pre-selected file path. Initiate the camera to start to acquire actual image frames. Execute a loop sequence where, in each loop, one frame is acquired, and subtracted (simple and absolute subtraction) from background image. Accumulate all acquired frames and produce the .AVI format files for all image process results. Based on selected attributes, process and display histograms for all produced images. Obtain statistical information from a selected area of the image. Process and display image edge detection. This sub-block will stay running the loop until a “stop” event is <i>true</i> .	Figure 46
4 <sup>th</sup>	Close the camera acquisition and finalize the production of all .AVI format files.	Figure 47

Having assembled and tested all components of the experimental setup, its resolution has to be characterized by defining and measuring some figures of merit in order to verify the compatibility of the readout setup with the sensor array and its imaging system. This step is very important to validate all the work of assembling.

THIS PAGE INTENTIONALLY LEFT BLANK



## IV. OPTICAL READOUT CHARACTERIZATION

This chapter is dedicated to identifying, understanding, and quantifying the figure of merit of the optical readout resolution in terms of gray-level value changes in the image per sensor deformation degree. A methodology to provide improvement and tuning of the readout to accommodate different sensor characteristics is also proposed.

### A. SETUP RESOLUTION ESTIMATION METHOD

An optical readout for microcantilever sensors can have several configurations depending on the components, sensor's dynamics, and sensor's size. Thus, it is important to characterize the resolution in order to verify the compatibility between the readout and the sensor. A methodology has been established to obtain the resolution in terms of the sensor's displacement in degrees per gray value of the image based on experimental measurements.

For the characterization, an available bi-material sensor array optimized for IR was used and is depicted in Figure 28. The fact that this sensor array does not work in THz range does not compromise the method procedure because the readout responds to resonant cavity bending and, therefore, it is independent of the radiation frequency used to induce the thermo-dynamic movement.

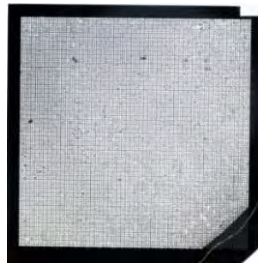


Figure 28. Picture of the array used in the characterization method proposed in this work. It has 120 x 120 sensors. After [13]

To obtain the resolution of the setup, first the mechanism to control the sensor temperature was defined. Control of temperature, in turn, allows control

over the sensor bending. A heater powered by a stabilized power source was used to control temperature. The foil heater is a model HT10K, 1" x 3" foil heating element with an acrylic pressure-sensitive adhesive backing and an integrated 10 k $\Omega$  Negative Temperature Coefficient (NTC) Thermistor temperature sensor (Figure 29) [51].



Figure 29. Picture of an HT10K Foil Heater produced by Minco Co., used to control the temperature of the sensor during the characterization procedure. From [52]

To monitor the heater temperature, the thermistor resistance was continuously measured during the characterization procedure using a multimeter. To convert thermistor resistance information in Kelvins, an electronic table developed by Dada was used [53]. The foil heater was bonded on a copper plate in order to provide good support to the sensor. The setup used to control the temperature over the sensor is depicted in Figure 30.

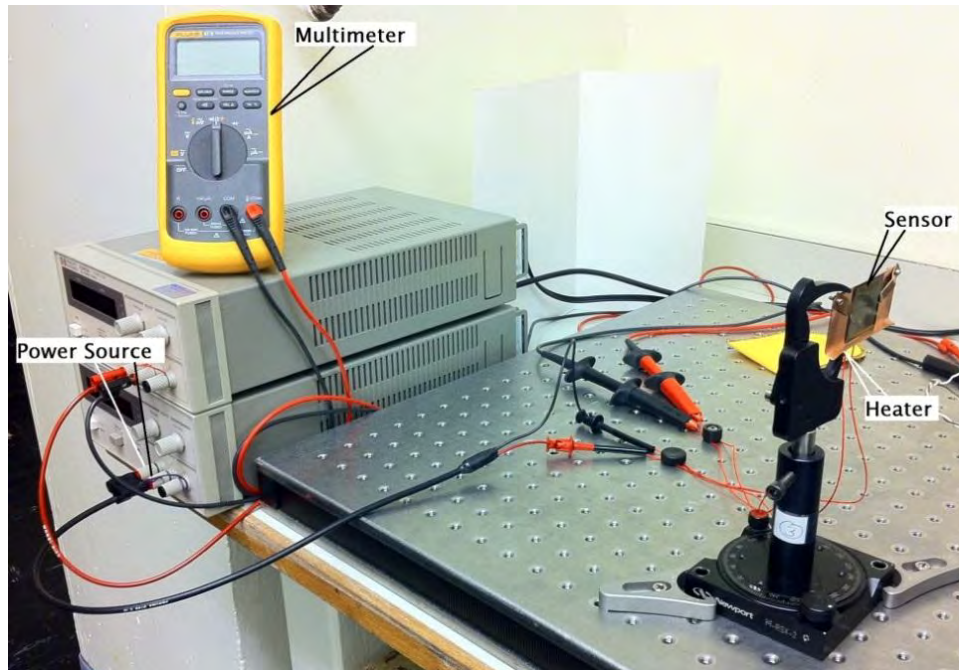


Figure 30. Setup used to control the temperature over the sensor array. The sensor array can be observed fixed on the copper plate that is wired to the power source and the multimeter. The multimeter monitors the heater temperature.

Having the temperature over the sensor array controlled, different temperatures were applied to the sensors; then measurements of individual sensor displacement were made. The characterization measurements were divided into two steps: (1) Sensor Characterization and (2) Readout Characterization. These two steps used two different assembly setups that are described in the following sections.

## 1. Sensor Characterization

In these measurements, the displacement of the sensor's resonant cavity was observed and measured using a microscope.

### a. Procedure

The sensor array was placed in close contact with the heater, the temperature was varied, and the sensor's deformation obtained by measuring the

distance from the microscope to the points on the resonant cavity surface. This was achieved by focusing the microscope on two points on the opposite ends of the resonant cavity (Figure 31) of the sensor. Both points were measured at the same temperature. The bending displacement is obtained by directly reading the microscope scale for the difference in height between the measured points. By dividing height difference by the resonant cavity length, and using the approximation that  $\sin(\theta) \sim \theta$  for small angles, the angular displacement can be obtained.

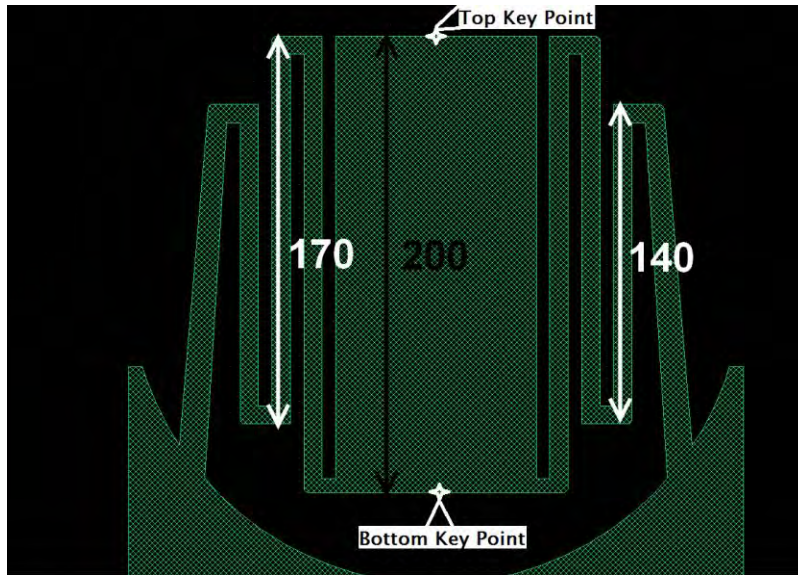


Figure 31. Sensor's dimensions and indication of the measured Key Points position. The difference between the heights of both indicated points provides the angular displacement of the resonant cavity. After [38].

Before starting the measurements, the sensors' physical conditions were verified in order to avoid the use of sensors that have visible damage in their structures. Four sensors of the array were randomly chosen to test the measurement procedure. In Figure 32, the setup used to make the sensor characterization can be observed.

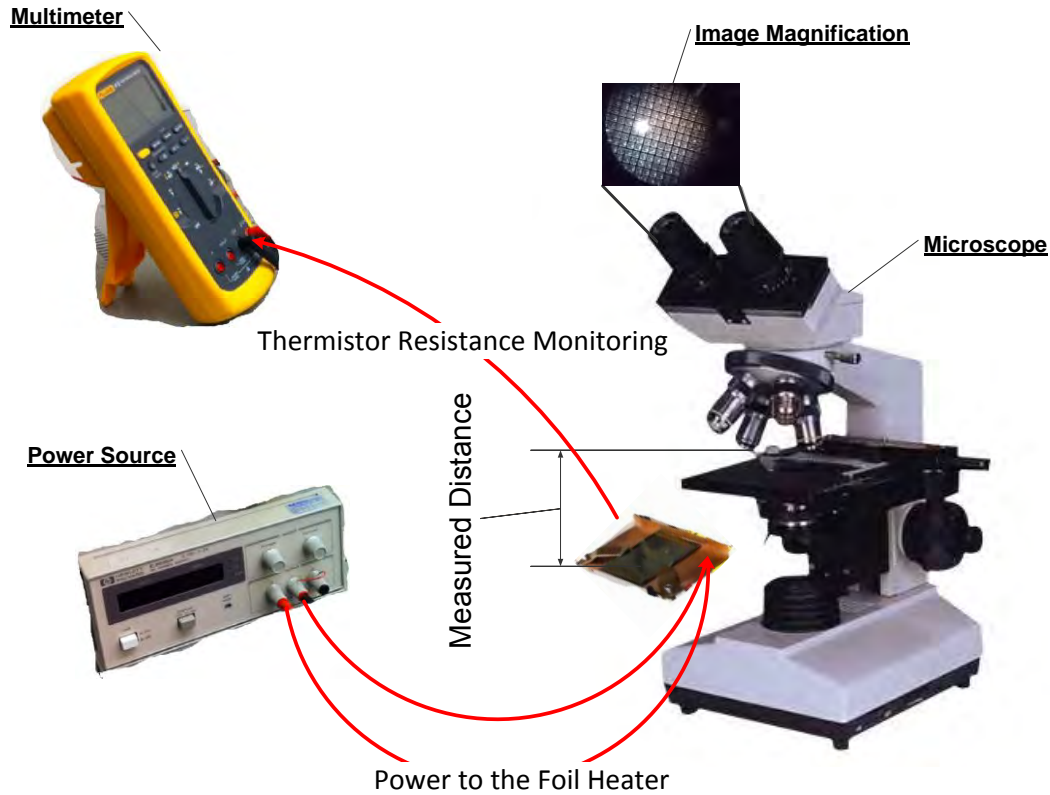


Figure 32. Sensor Characterization setup scheme. The microscope is used to measure the distance between the microscope lens and the key points over the resonant cavity; the difference between these two distances, divided by the resonant cavity length, gives the sensor's angular deflection at a given temperature.

From the displacement data, the information of the sensors' deflection in terms of degrees per Kelvin units was obtained.

### ***b. Results***

All measurements were recorded in micrometers ( $\mu\text{m}$ ). Having the longitudinal size of the microcantilever ( $200 \mu\text{m}$ ) and the difference between the two measured key points, the angle of the microcantilever at each respective temperature was computed. The data is plotted in Figure 33, where clearly can be observed four clusters of data that represent each measured sensor.

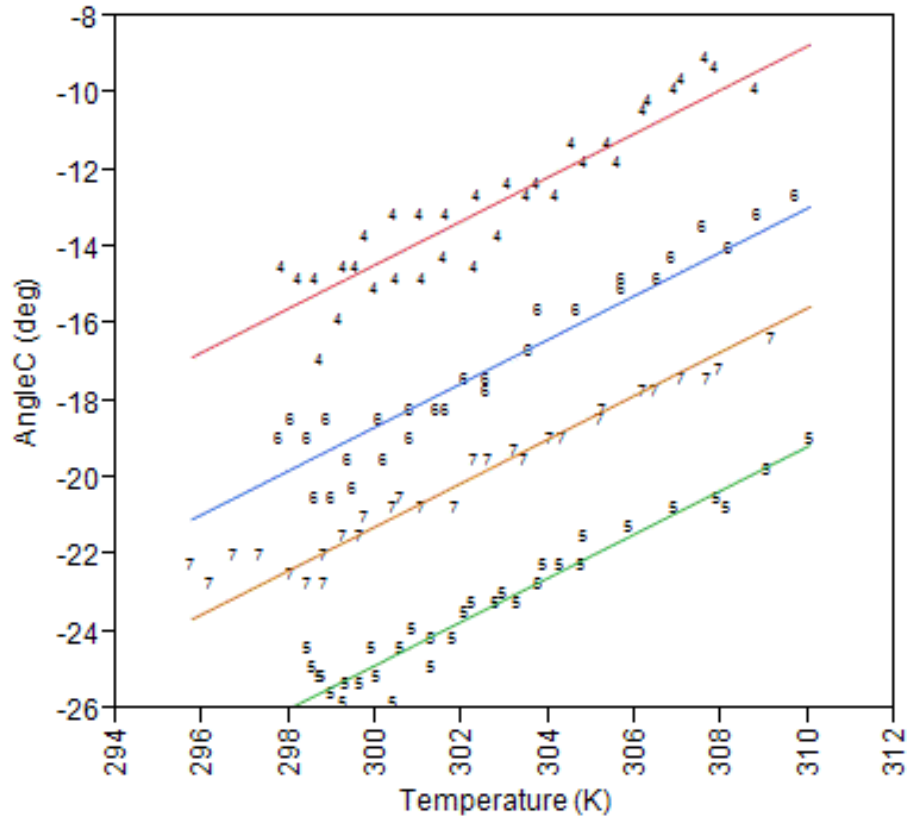


Figure 33. Plot of data from Sensor Characterization procedure. Each line on the plot represents a linear fit over the data obtained from each sensor. A very similar angular deflection per unit Kelvin between the measured sensors can be observed.

Considering the expected linearity of response for the sensors [10], a linear fit to check the similarity between the sensors' behavior was made. In Figure 33, their lines can be seen having almost the same slope, which means homogeneity in deflection per unit of temperature and consistency of the measurement procedure.

Using the software JMP Pro [54], a simple regression one-way analysis of variance was done to test whether there was a difference in mean response between four pixels, and to obtain the slope for sensor response and the error associated with the measurements. The graphical analysis is shown in Figure 34.

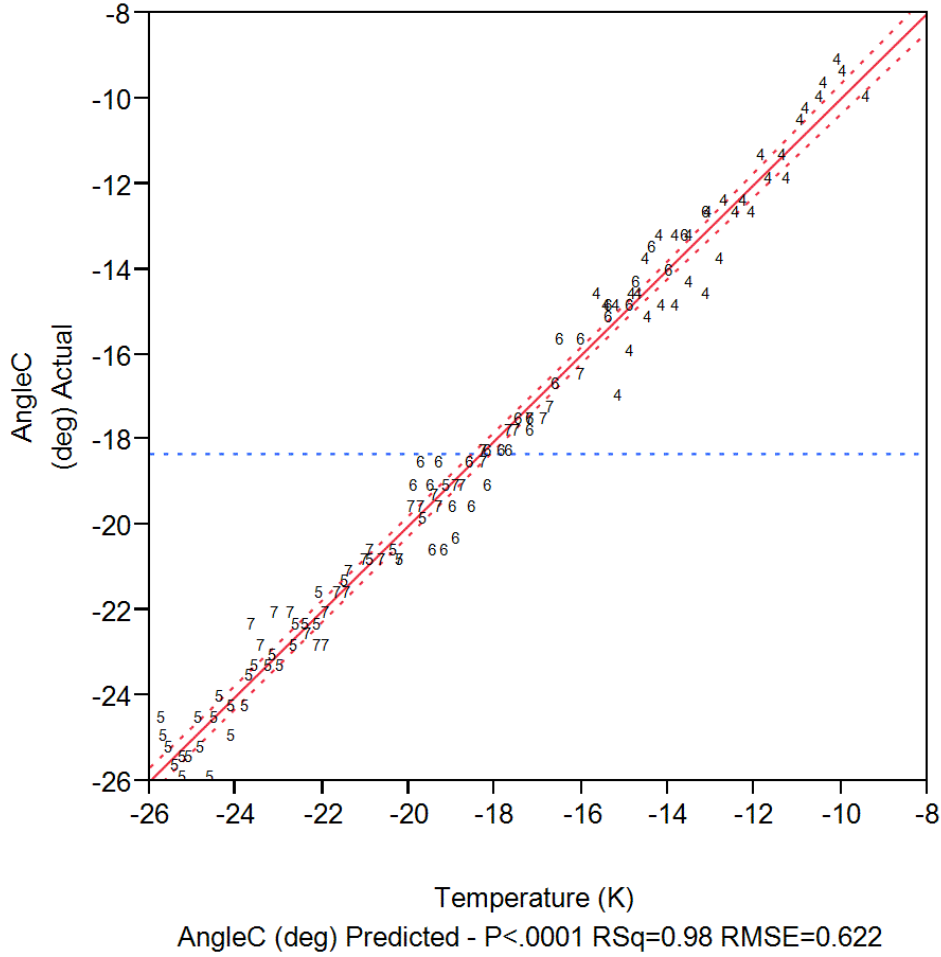


Figure 34. Data regression from the sensor characterization procedure where common behavior parameters are computed for all data.

Figure 34 shows the value of the root square (RSq), which means that 98% of the variation in the response could be absorbed by fitting the used model. The Root Mean Square Error (RMSE) equals 0.622, which means the standard deviation of the random error of the obtained data, and the  $P < 0.0001$  ( $p$  value) confirms significant regression factors in the model. From the regression, the slope and the standard error for the model were also obtained. From that information, it could be concluded that the sensor response (SR) for temperature variance is:

$$SR = 0.569 \text{ } ^\circ\text{C/K}, (\text{Std.Error} = 0.016, \text{ or } \pm 0.032 (95\%)) \quad (1)$$



The computed value is not far from the displacement rate estimated by Grbovic [10] of  $0.299 \text{ }^{\circ}\text{K}$ , which actually represents a better response to the temperature variance.

## **2. Readout Characterization**

Unlike the sensor characterization, in this procedure the displacement of the sensor was not measured but, rather, the intensity of the beam reflected by a single sensor's pixel over the CCD camera. For this characterization, the intensity of the beam is the mean intensity, in 255 gray-value levels, of the area of the CCD that represents the image of one sensor (resonant cavity and legs) in the array.

### ***a. Procedure***

To vary the temperature, the same temperature control setup was used as in sensor characterization but positioned in the optical readout setup as shown in Figure 30.

Before starting the measurements, the sensor array was aligned in the readout setup in order to obtain bright spots from the pixels on the CCD. That position was checked by observing the image on the software application. Then, one bright spot on the current image display and its area were selected to obtain statistical information from the image pixels. In this case, all selected areas had the dimension of 8 x 8 pixels. Having the camera setup ready, and having identified the selected area around a bright spot, the application was restarted and temperature changes were applied to the sensor. As the temperature changed, the brightness of the spot varied, and all mean intensity values of the spot's area as the temperature related to that intensity were recorded. All these measurements were performed over subtracted images; thus, the procedure began with very low values and went to bright spots as the temperature increased and decreased.



From this measurement procedure, information about beam intensity of a reflected beam from one sensor over the CCD in terms of gray-value per Kelvin units could be obtained.

### ***b. Results***

For this second step, valid results from two sensors could be obtained. Using the optical readout, sensors were chosen based on well-observed variations in brightness of one sensor in an area of 8 x 8 image pixels. All obtained spot-brightness data was recorded in grayscale values jointly with temperature levels in Kelvin. All data was plotted in a graphical representation shown in Figure 35 where two discrete clusters that represent the measured sensors can be observed.

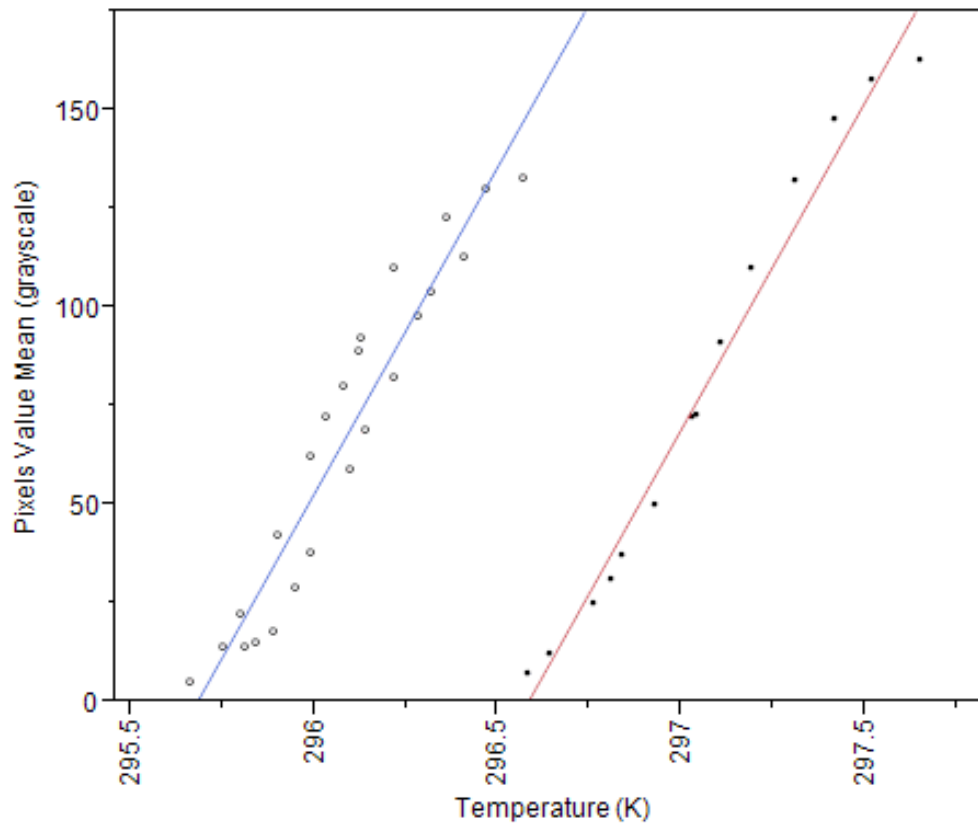


Figure 35. Plot of data from readout-characterization procedure. Each solid line on the plot represents a linear fit over the data obtained from each sensor. A very similar behavior between two sensors analyzed can be observed.

As were done with sensor characterization data, the clusters were also fitted linearly to check the consistency between the behavior of the two sensors, and it can be observed from Figure 35 that both measurements have linear response with similar slopes.

Following the same procedure as performed in the sensor characterization, and also using the software JMP Pro [54], a simple one-way regression analysis of variance was done to test whether there was a difference in mean response between two sensors, and to obtain the slope for the sensors' response and the error associated with the measurements. The graphical analysis is shown in Figure 36.

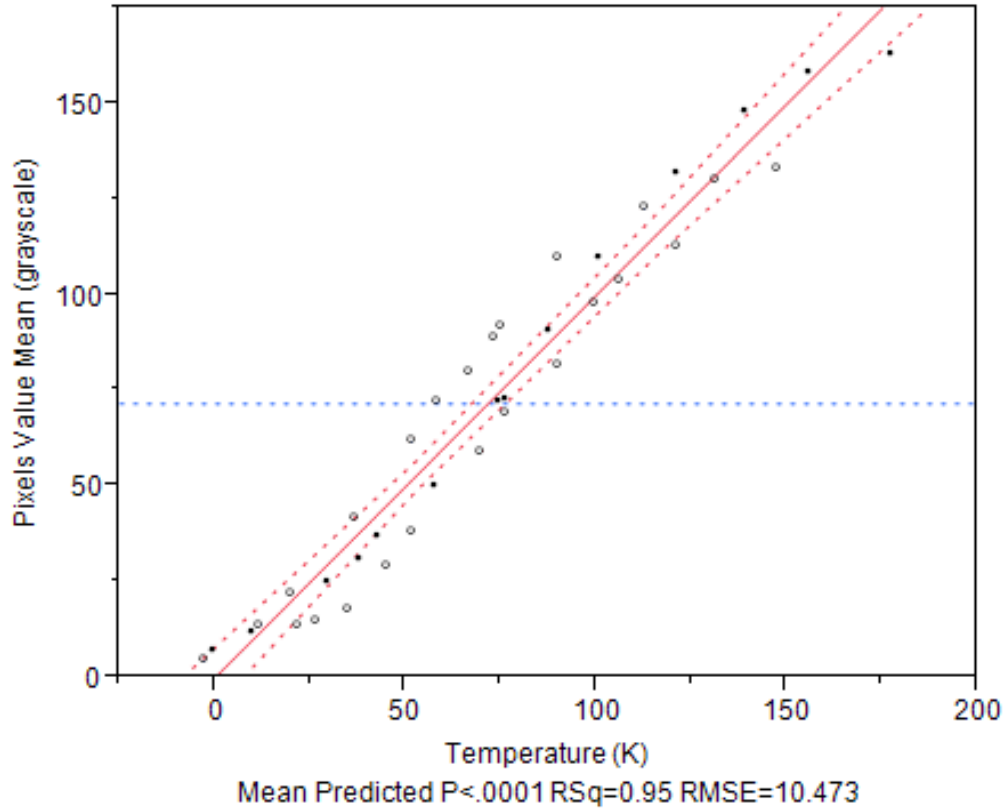


Figure 36. Data regression from readout characterization procedure where common behavior parameters are computed for all data.

Figure 36 shows the value of root square (RSq) that means 95% of the variation in the response could be accounted for by fitting the used model. The root mean square error (RMSE) equals 10.473 means the standard deviation of the random error of the obtained data, and the  $P < 0.0001$  confirms the evidence that there are significant regression factors in the model. From the regression, the slope and the standard error for the model were also obtained, from which could be concluded that the readout response ( $RR$ ) for temperature variance is:

$$RR = 165.624 \text{ Gray-value} / \text{K}, (\text{Std.Error} = 6.351, \text{ or } \pm 12.448(95\%)) \quad (2)$$

It is noteworthy that the slope value that represents the amount of gray-value levels came from the subtraction of the background from the actual image of the observed spot.

## B. READOUT ANALYSIS

Finally, it is possible to obtain the resolution of the readout by combining the results obtained from sensor and readout characterizations.

All obtained data confirmed the expected behavior for the sensor and optical readout. The objective of the method is to obtain the resolution of the optical readout setup for such given conditions. Based on obtained results, the values can be joined, the temperature dependency can be eliminated, and the minimum angular deformation of the resonant cavity registered by one gray value can be computed. Thus, from Equations (1) and (2), the readout resolution ( $RRes$ ) can be computed:

$$RRes = \frac{0.569}{165.624} = 3.433 \text{ mdeg} / \text{Gray-value}, (\pm 0.323) \quad (3)$$

Therefore, the same setup resolution value can be expected for any sensor that has the same resonant cavity size, no matter what its bending response to THz radiation exposure is.

### C. OPTICAL READOUT AND THZ IMAGING SYSTEM INTEGRATION

The optical readout design proposed in this work has to be integrated with the THz imaging system under development at NPS, which is schematically shown in Figure 37.

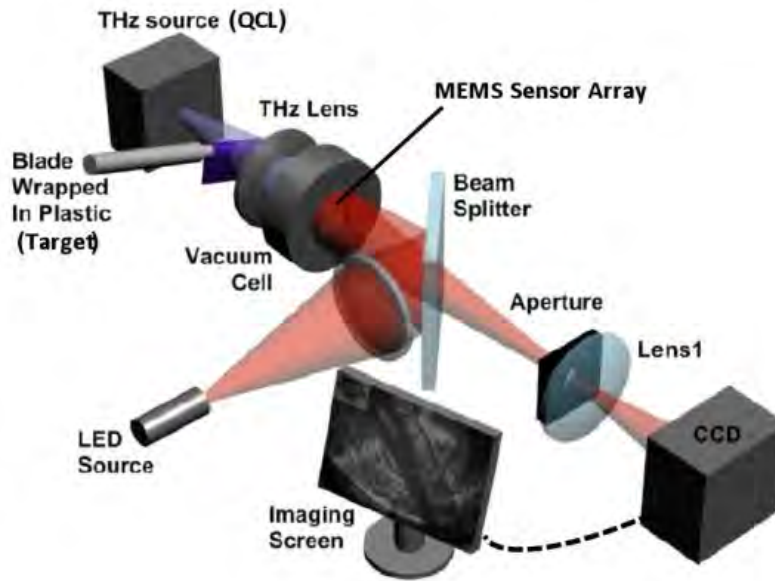


Figure 37. THz Imaging System setup scheme being developed in the NPS Sensor Laboratory. After [13].

Considering that the sensor array needs to remain inside a vacuum chamber during the operation, as reported by Grbovic [10], it is important to consider the dimensions of such a chamber in order to allow the illumination of all areas of the sensor array, without visible light beam reflections from its windows. The vacuum chamber should be fixed on a rotating mount (shown in Figure 18) to allow the initial alignment of the sensor for the background reference image capture.

A very important step in integration is to characterize the sensor array deflection under QCL illumination of the imaging system. To perform this characterization the same procedure as described in Section A.2. of this chapter

has to be followed after first aligning the array without THz illumination to acquire the background reference image. Next, the QCL has to be turned on to obtain the subtracted image with the sensor at maximum deflection. The subtracted image obtained in this characterization has to be analyzed by the user to verify whether the brightness spots in the image have enough contrast to allow a well-defined image of the target shape. Otherwise, the readout has to be adjusted to increase its resolution.

If any increment in resolution of the readout is necessary, the setup arrangement has to be modified and the characterization procedures repeated. The most significant modification to be made in the readout setup, which should increase its resolution, is the total distance between the CCD and the sensor array. Modifying that distance, the user has to consider all aspects described in Chapter III, and also take into account the following:

- The beam from the light source has to illuminate the whole sensor array area;
- The aperture control 2 does not have to be modified to change the aperture diameter, but its distance to the lens 2 has to be adjusted in order to place the aperture at the spectrum plane;
- Lens 3 and the camera have to be repositioned to obtained image in focus; and,
- No adjustments in software would be necessary.

After these adjustments and another characterization procedure, if the resolution is not improved to address imaging needs, replacement or improvement of components or modifications in image software post-processing tools would be necessary; and, for that, new studies would be required.

The readout should be tuned for each sensor array that has a different structure dimension or configuration than the one reported in this work. For such characterization, the method described in this chapter has to be followed, and the results have to be analyzed and compared to the expected dynamic behavior of the sensors under THz illumination.

THIS PAGE INTENTIONALLY LEFT BLANK

## **V. CONCLUSIONS**

THz radiation is becoming an important tool in the field of imaging because of its distinctive properties and its relevance for applications in medicine and security. Multiple works, research reports, and products are appearing every day presenting new technologies and tools for all kinds of applications in the THz frequency region.

Driven by the current research of the Sensor Research Laboratory at NPS related to design and fabrication of THz-optimized bi-material MEMS sensor arrays for THz imaging, this work was intended to contribute to the efforts to achieve a readout system to measure sensor array responses.

Chapter II had a focused discussion about bi-material THz sensor arrays wherein were presented the principle of operation and the architectural design for the sensor array.

Chapter III presented the concept for an optical readout for bi-material sensors, and explained the configuration and limitation of multiple sensors–probing configuration.

Chapter IV has details of the multiple sensors–probing optical readout that was designed and assembled for this work. The subsystems, hardware components, and the CCD camera software control were also presented.

Chapter V was dedicated to describing a methodology established to estimate the resolution of the readout. All results obtained following the methodology were analyzed, and the possibilities and consequences of the integration of the optical readout into a THz imaging system were discussed.

After the performed work, some aspects were identified that could lead to improvement and optimization for the readout performance. Those aspects were not addressed because they were outside the objective of this work or beyond the limited time and resources of the research. However, the following approaches are suggested for future work and investigations.

Improvements on the set of lenses used in the readout system should strive to minimize distortions and aberrations and make the readout setup more compact. The first step to getting those improvements would be a simulation of the setup with some kind of computational tool that allows researchers to play with components' positioning in search of an optimized readout performance.

Depending on the objective of an imaging system, the image post-processing could be very relevant for obtaining the right image. Exploring more possibilities of extracting information from the readout in different formats is suggested and exploring other computational resources that can modify more image parameters, allowing a better use of the results.

If compactness becomes an issue, modifications to component configuration could take advantage of the configuration reported by Salerno [33], but probably that brings implications that would require precautions to avoid readout performance reduction.

In this work, what the CCD camera frame rate should be as compared to the sensor response time could not be quantified since there was not the opportunity to complete the integration of the optical readout into the THz imaging system. That sensitivity and size of the CCD are probably the key points to be considered in order to have greater fps from the camera without modifications in the diameter of Aperture 2. Another aspect is that the fps of the camera has to be proportional to the time response of the sensor in order to not increase the cost unnecessarily. The frame-rate acquisition would be a relevant issue depending on the application of the system. Thus, studies to establish a method to characterize this figure of merit that can work as the basis for readout design adjustments are suggested.

Finally, the objective of presenting an optical readout setup for bi-material microcantilever sensors and characterizing its resolution following one specific method of measurement was fulfilled.



## LIST OF REFERENCES

- [1] B. S. Ferguson, S. Wang, H. Zhong, D. Abbott, and X.-C. Zhang, "Powder detection with T-ray imaging," in *Proceedings of SPIE*, Orlando, FL, USA, 2003, pp. 7–16.
- [2] Laboratory of Terahertz Spectroscopy, Prague, "Spectrum of Electromagnetic Radiation," *Introduction*, 05-Apr-2011. [Online]. Available: <http://department.fzu.cz/lts/en/intro.htm>. [Accessed: 05-Aug-2011].
- [3] B. Dumé, "Power from terahertz beams," *physicsworld.com*, 14-Nov-2002. [Online]. Available: <http://physicsworld.com/cws/article/news/16414>. [Accessed: 12-Aug-2011].
- [4] P. Shumyatsky and R. R. Alfano, "Terahertz sources," *Journal of Biomedical Optics*, vol. 16, no. 3, p. 033001, 2011.
- [5] DOE/Argonne National Laboratory, "New T-ray source could improve airport security, cancer detection," *ScienceDaily*. [Online]. Available: <http://www.sciencedaily.com/releases/2007/11/071126121732.htm>. [Accessed: 27-Jul-2011].
- [6] CERN, "JLab generates high-power terahertz light," *CERN Courier*, 01-Jan-2003. [Online]. Available: <http://cerncourier.com/cws/article/cern/28777>. [Accessed: 29-Jul-2011].
- [7] R. Miles and NATO Advanced Research Workshop on Terahertz Frequency Detection and Identification of Materials and Objects, *Terahertz frequency detection and identification of materials and objects*. Dordrecht (The Netherlands): Springer, 2007.
- [8] P. H. Siegel, "Terahertz technology," *IEEE Transactions on Microwave Theory and Techniques*, vol. 50, no. 3, pp. 910–928, Mar. 2002.
- [9] T. Yasuda, Y. Kawada, H. Toyoda, A. Nakanishi, K. Akiyama, and H. Takahashi, "Fast frequency-resolved terahertz imaging," *Review of Scientific Instruments*, vol. 82, no. 3, p. 034708, 2011.
- [10] D. Grbovic, "Imaging by Detection of Infrared Photons Using Arrays of Uncooled Micromechanical Detectors," PhD dissertation, University of Tennessee, 2008.
- [11] Y.-S. Lee, *Principles of terahertz science and technology*. New York: Springer, 2009.

- [12] B. A. Knyazev, M. A. Dem'yanenko, and D. G. Esaev, "Terahertz imaging with a 160x120 pixel microbolometer 90-fps camera," in *IRMMW-THz. Joint 32nd International Conference on Terahertz Electronics*, Cardiff, UK, 2008, pp. 360–361.
- [13] D. Grbovic and G. Karunasiri, "Fabrication of Bi-material MEMS detector arrays for THz imaging," in *Proceedings of SPIE*, Orlando, FL, USA, 2009, vol. 7311, pp. 731108-1 731108-7.
- [14] D. Doodley, "Measuring THz Radiation...choose a Pyroelectric Detector or Golay Cell? - Application Note." Spectrum Detector, Inc., 25-May-2009.
- [15] Microtech Instruments, Inc., "THz Detectors - Golay Cells – Datasheet," *Catalog and Datasheet Downloads*, 2011. [Online]. Available: <http://www.mtinstruments.com/downloads/Golay%20Cell%20Datasheet%20Revised.pdf>. [Accessed: 17-Aug-2011].
- [16] H.-W. Hübers, "Active Terahertz Imaging for Security (TeraSec)," Berlin, 27-Mar-2007.
- [17] X. Zheng, C. V. McLaughlin, P. Cunningham, and L. M. Hayden, "Organic Broadband TeraHertz Sources and Sensors," *Journal of Nanoelectronics and Optoelectronics*, vol. 2, no. 1, pp. 1–19, Apr. 2007.
- [18] D. H. Auston, "Picosecond optoelectronic switching and gating in silicon," *Applied Physics Letters*, vol. 26, no. 3, p. 101, 1975.
- [19] D. H. Auston, K. P. Cheung, and P. R. Smith, "Picosecond photoconducting Hertzian dipoles," *Applied Physics Letters*, vol. 45, no. 3, p. 284, 1984.
- [20] Q. Wu and X.-C. Zhang, "Free-space electro-optic sampling of terahertz beams," *Applied Physics Letters*, vol. 67, no. 24, p. 3523, 1995.
- [21] A. Schneider, M. Stillhart, and P. Günter, "High efficiency generation and detection of terahertz pulses using laser pulses at telecommunication wavelengths," *Optics Express*, vol. 14, no. 12, p. 5376, 2006.
- [22] Thermo Nicolet, Co., "Introduction to Fourier Transform Infrared Spectrometry," *Molecular Materials Research Center*, 2001. [Online]. Available: <http://mmrc.caltech.edu/FTIR/FTIRintro.pdf>. [Accessed: 17-Aug-2011].
- [23] W. L. Chan, J. Deibel, and D. M. Mittleman, "Imaging with terahertz radiation," *Reports on Progress in Physics*, vol. 70, no. 8, pp. 1325–1379, Aug. 2007.

- [24] P. Y. Han, M. Tani, M. Usami, S. Kono, R. Kersting, and X.-C. Zhang, "A direct comparison between terahertz time-domain spectroscopy and far-infrared Fourier transform spectroscopy," *Journal of Applied Physics*, vol. 89, no. 4, p. 2357, 2001.
- [25] R. Bogue, "Terahertz imaging: a report on progress," *Sensor Review*, vol. 29, no. 1, pp. 6–12, 2009.
- [26] B. B. Hu and M. C. Nuss, "Imaging with terahertz waves," *Optics Letters*, vol. 20, no. 16, p. 1716, Aug. 1995.
- [27] R. Amantea, "Progress toward an uncooled IR imager with 5-mK NETD," in *Proceedings of SPIE*, San Diego, CA, USA, 1998, pp. 647–659.
- [28] P. I. Oden, P. G. Datskos, T. Thundat, and R. J. Warmack, "Uncooled thermal imaging using a piezoresistive microcantilever," *Applied Physics Letters*, vol. 69, no. 21, p. 3277, 1996.
- [29] T. W. Kenny et al., "Micromachined infrared sensors using tunneling displacement transducers," *Review of Scientific Instruments*, vol. 67, no. 1, p. 112, 1996.
- [30] P. G. Datskos, "Micromechanical uncooled photon detectors," in *Proceedings of SPIE*, San Jose, CA, USA, 2000, pp. 80–93.
- [31] Yang Zhao et al., "Optomechanical uncooled infrared imaging system: design, microfabrication, and performance," *Journal of Microelectromechanical Systems*, vol. 11, no. 2, pp. 136–146, Apr. 2002.
- [32] T. Cheng, Q. Zhang, B. Jiao, D. Chen, and X. Wu, "Optical readout sensitivity of deformed microreflector for uncooled infrared detector: theoretical model and experimental validation," *Journal of the Optical Society of America. A, Optics, Image Science, and Vision*, vol. 26, no. 11, pp. 2353–2361, Nov. 2009.
- [33] J. P. Salerno, "High frame rate imaging using uncooled optical readout photomechanical IR sensor," in *Proceedings of SPIE*, Orlando, FL, USA, 2007, vol. 6542, p. 65421D-65421D-9.
- [34] P. G. Datskos and N. V. Lavrik, "Uncooled Infrared MEMS Detectors," in *Smart Sensors and MEMS*, vol. 181, S. Y. Yurish and M. T. S. R. Gomes, Eds. Dordrecht: Springer Netherlands, 2004, pp. 381–419.
- [35] P. G. Datskos, "Optical Readout of MEMS," in *IRIS Material Meeting Proceedings*, Knoxville, TN, 16-Aug-1999

- [36] L. R. Senesac, J. L. Corbeil, S. Rajic, N. V. Lavrik, and P. G. Datskos, "IR imaging using uncooled microcantilever detectors," *Ultramicroscopy*, vol. 97, no. 1-4, pp. 451–458, 2003.
- [37] Z. Guo et al., "Performance analysis of microcantilever arrays for optical readout uncooled infrared imaging," *Sensors and Actuators A: Physical*, vol. 137, no. 1, pp. 13-19, Jun. 2007.
- [38] D. Grbovic, "Pixel Dimensions Figure," [E-mail: 31-May-2011].
- [39] J. Zhao, "High sensitivity photomechanical MW-LWIR imaging using an uncooled MEMS microcantilever array and optical readout (Invited Paper)," in *Proceedings of SPIE*, Orlando, FL, USA, 2005, pp. 506–513.
- [40] Q. Zhang et al., "Optical readout uncooled infrared imaging detector using knife-edge filter operation," *Optoelectronics Letters*, vol. 3, no. 2, pp. 119-122, Mar. 2007.
- [41] National Instruments Corporation, *LabVIEW 2010 Professional Development System*. USA. National Instruments Corporation, 2010.
- [42] Cree, Inc, "Product Family Data Sheet - Cree XLamp XP-E LEDs." *Product Information*. [Online]. Available: <http://www.cree.com/products/pdf/xlampxp-e.pdf>. [Accessed: 19-Jul-2011].
- [43] superbrightleds.com, "XPE series Cree LED | Super Bright LEDs." *XPE series Cree LED*. [Online]. Available: <http://www.superbrightleds.com/moreinfo/component-leds/xpe-series-cree-led/325/1261/>. [Accessed: 19-Jul-2011].
- [44] Microtech Instruments, Inc., "Transmission Spectra of Tsurupica and Polyethylene," *Thz Lenses & Windows*. [Online]. Available: <http://www.mtinstruments.com/thzlenses/index.htm>. [Accessed: 14-Aug-2011].
- [45] Basler Vision Technologies, Inc., "Basler A630f - User's Manual," *Manuals*, 07-Dec-2010. [Online]. Available: [http://www.baslerweb.com/downloads/12065/A630f\\_Users\\_Manuals.pdf](http://www.baslerweb.com/downloads/12065/A630f_Users_Manuals.pdf). [Accessed: 22-Jul-2011].
- [46] Sony Corporation, "Sony ICX267AL – Datasheet," *Automated Imaging Cameras*, 01-Dec-2003. [Online]. Available: [http://www.1stvision.com/cameras/sensor\\_specs/ICX267.pdf](http://www.1stvision.com/cameras/sensor_specs/ICX267.pdf). [Accessed: 22-Jul-2011].

- [47] Basler Vision Technologies, "Camera Specification - Basler A631f - Measurement protocol using the EMVA Standard 1288," 02-Nov-2006. [Online]. Available: <http://crijolanta.com.pl/produkty/basler/a631f-emva.pdf>. [Accessed: 27-Jul-2011].
- [48] National Instruments, "What Is NI LabVIEW?," *Product Information*. [Online]. Available: <http://www.ni.com/labview/whatis/>. [Accessed: 24-Jul-2011].
- [49] T. Yasuda, Y. Kawada, H. Toyoda, and H. Takahashi, "Terahertz movie of internal transmission imaging," *Optics Express*, vol. 15, no. 23, p. 15583, 2007.
- [50] National Instruments Corporation, "NI Vision Concepts Help," Jan-2011. [Online]. Available: <http://digital.ni.com/manuals/372916.zip>. [Accessed: 24-Jul-2011].
- [51] Thorlabs, Inc., "HT10K -Foil Heating Element." [Online]. Available: <http://www.thorlabs.com/Thorcat/14000/14034-s01.pdf>. [Accessed: 23-Jul-2011].
- [52] Thorlabs, Inc., "HT10K Foil Heater with 10,000 Ohm Thermistor," *Thorlabs Resistive Heaters*, 2011. [Online]. Available: <http://thorlabs.com/thorProduct.cfm?partNumber=HT10K>. [Accessed: 24-Jul-2011].
- [53] B. Dada, *Setup Calculations for the Thermistor Slope in the Temperature Control Circuit*. New Jersey, USA,. Thorlabs, Inc., 2010.
- [54] SAS Institute Inc., *JMP Pro*. Cary, NC, USA: SAS Institute Inc., 2010.

THIS PAGE INTENTIONALLY LEFT BLANK

## APPENDIX A. CAMERA CONTROLS AND IMAGE ANALYSIS SOFTWARE PROCESSES FLOWCHARTS

The processes flowcharts describe the logical sequence of macro events executed by the software to control the camera used in the optical readout setup and to provide tools for image analysis to the operator. The camera setup process is shown in Figure 38 and has the objective of preparing the camera to begin the acquisition of image frames.

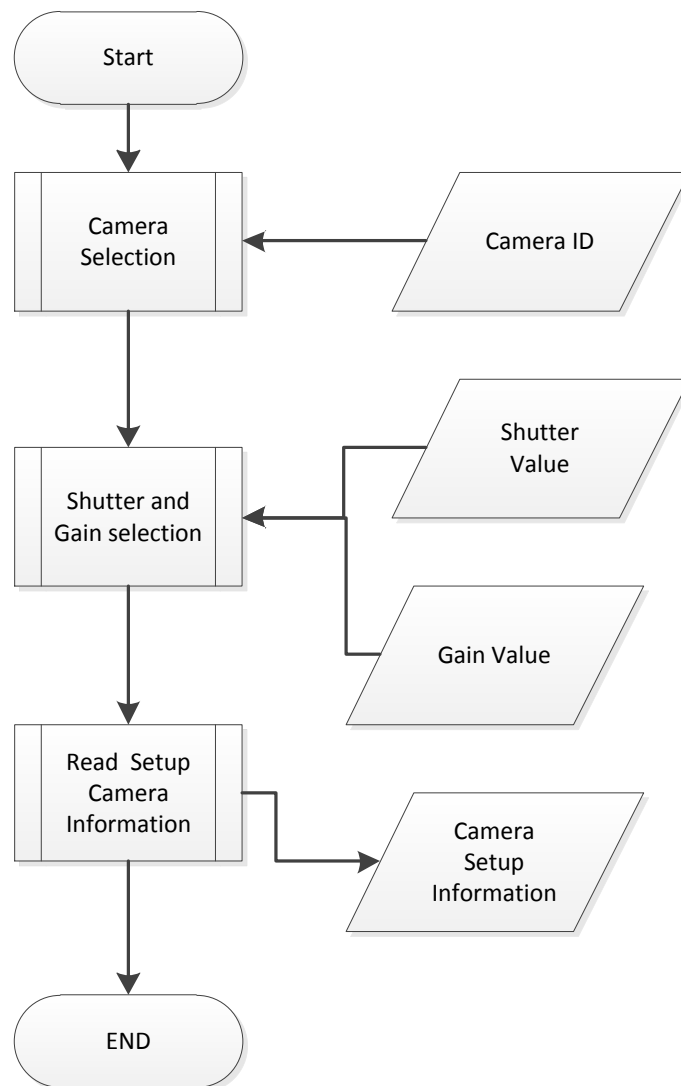


Figure 38. Camera setup process.

In the next process (Figure 39), the software executes the acquisition of a single frame that will be used as the background image reference for the real-time imaging.

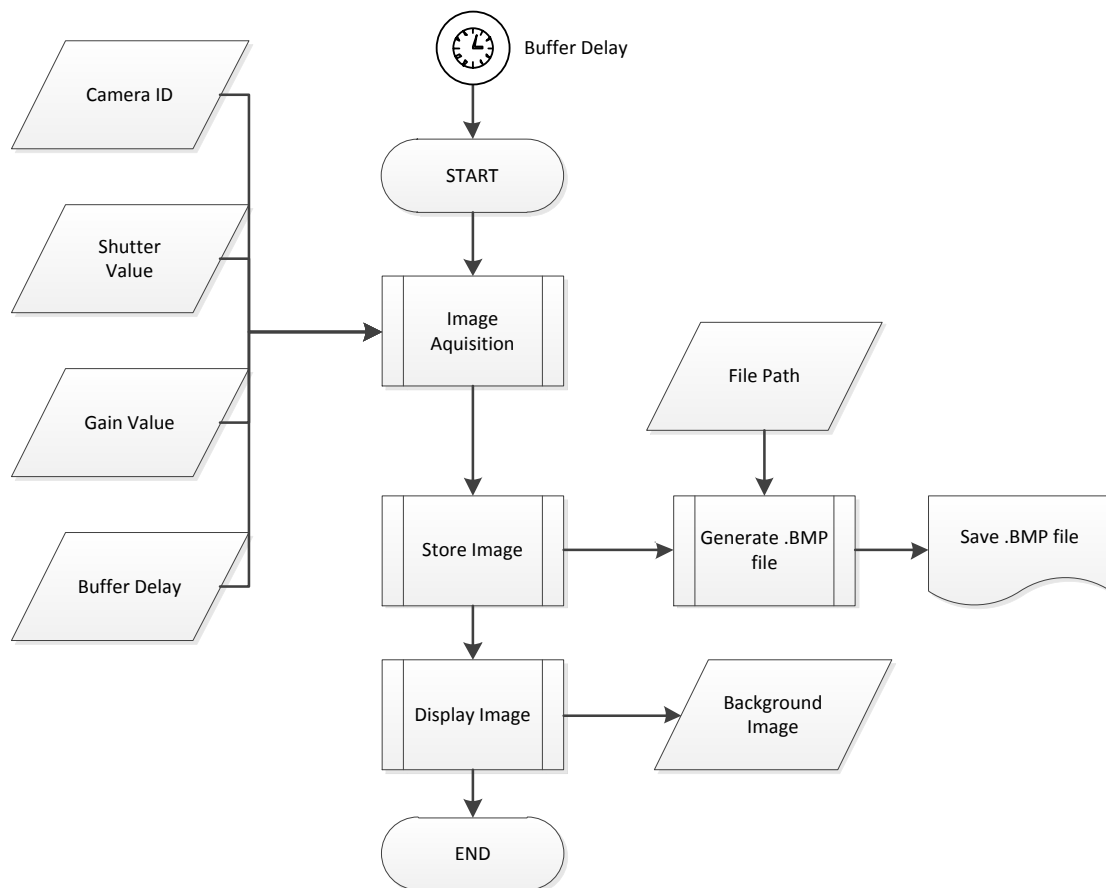


Figure 39. Background image frame acquisition process.



Having finished the process of background acquisition, the software initializes a continuous sequential imaging that is executed in a loop until a “stop” event occurs, as detailed in Figure 40.

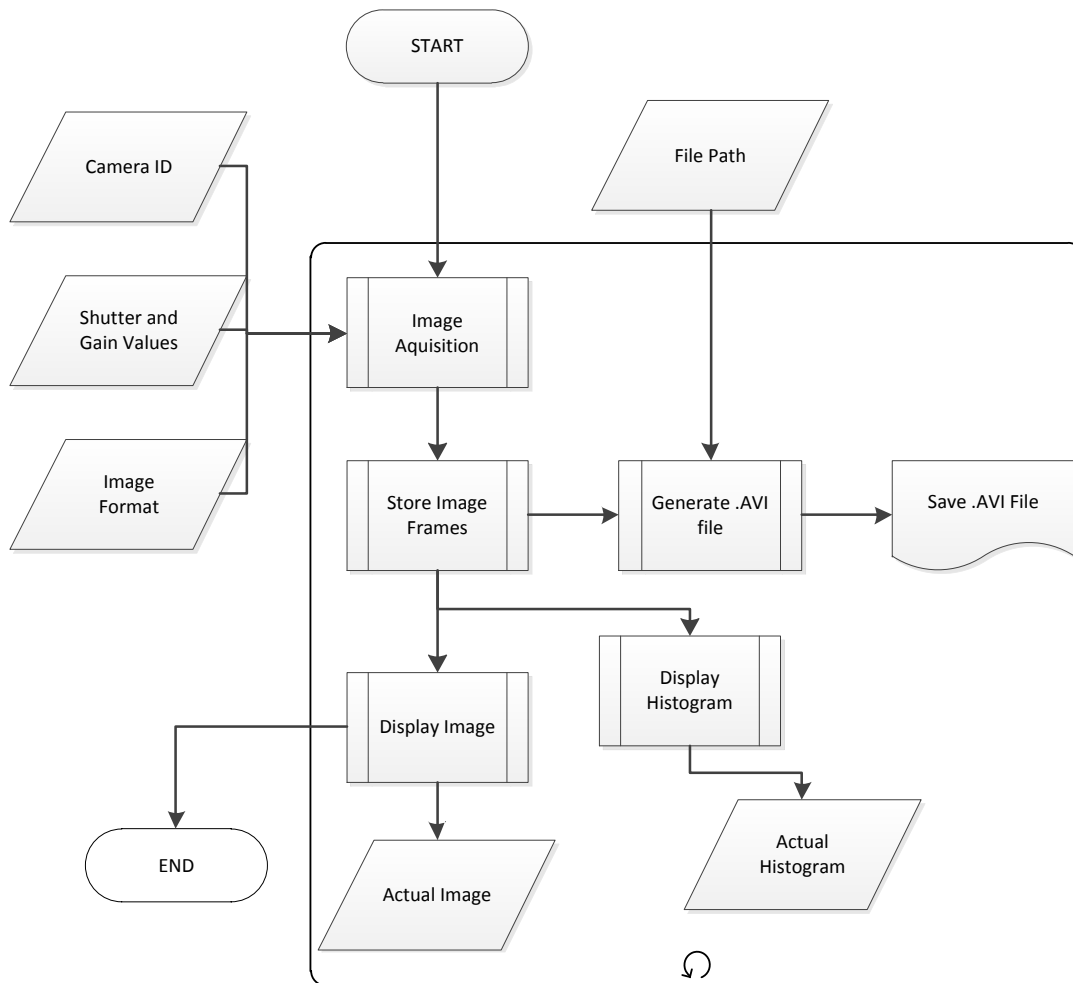


Figure 40. Sequential image frames acquisition process.

To provide readable information, the software automatically subtracts each subsequently acquired frame from the reference background image and presents the result to the operator in image format and its pixels' values in histograms. All results of this process are saved in the computer. These steps are shown in Figure 41.

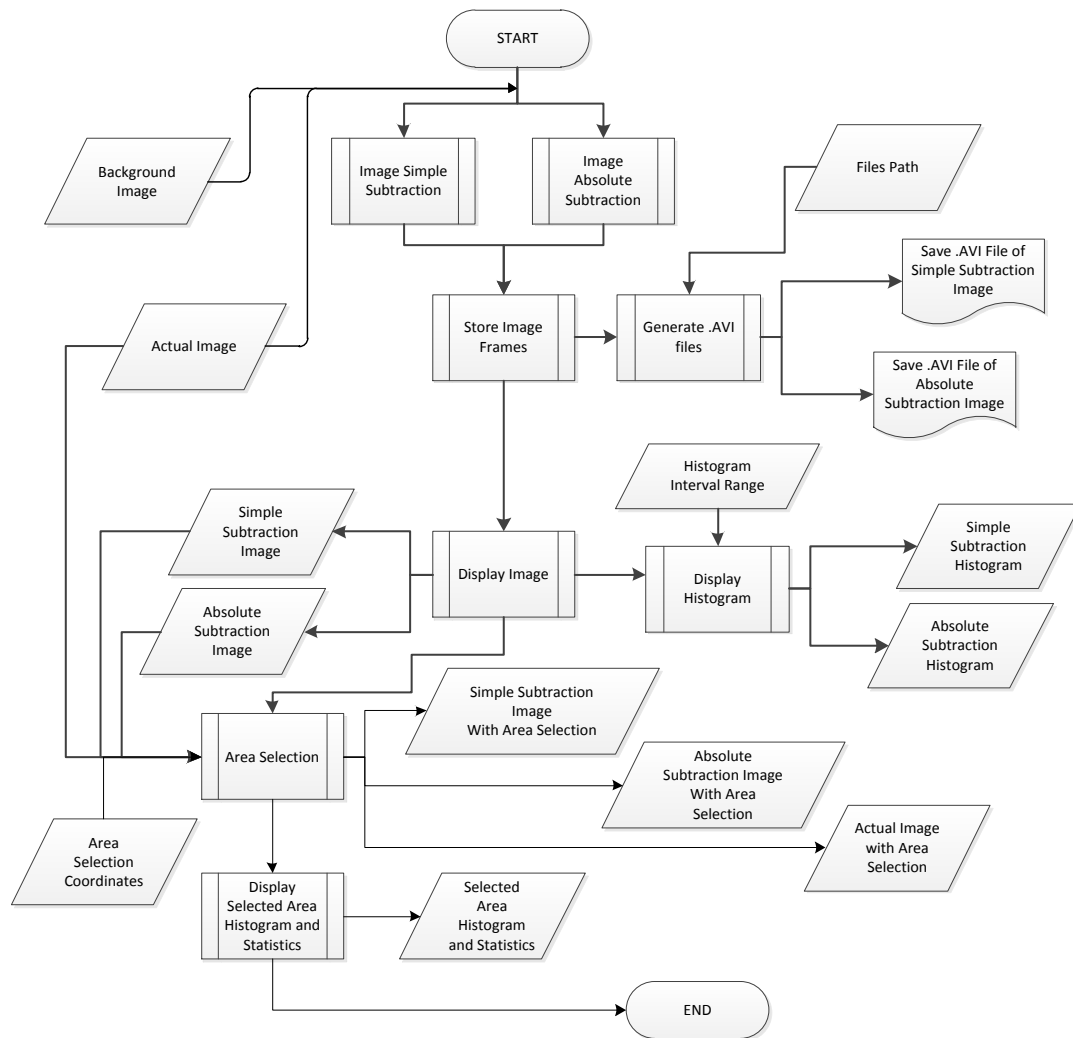


Figure 41. Subtracted images displaying process.

The process shown in Figure 42 provides an analysis tool that permits the operator to obtain pixel statistical values from an area over the image in the display chosen in his sole discretion. All results are updated continuously while the imaging acquisition persists.

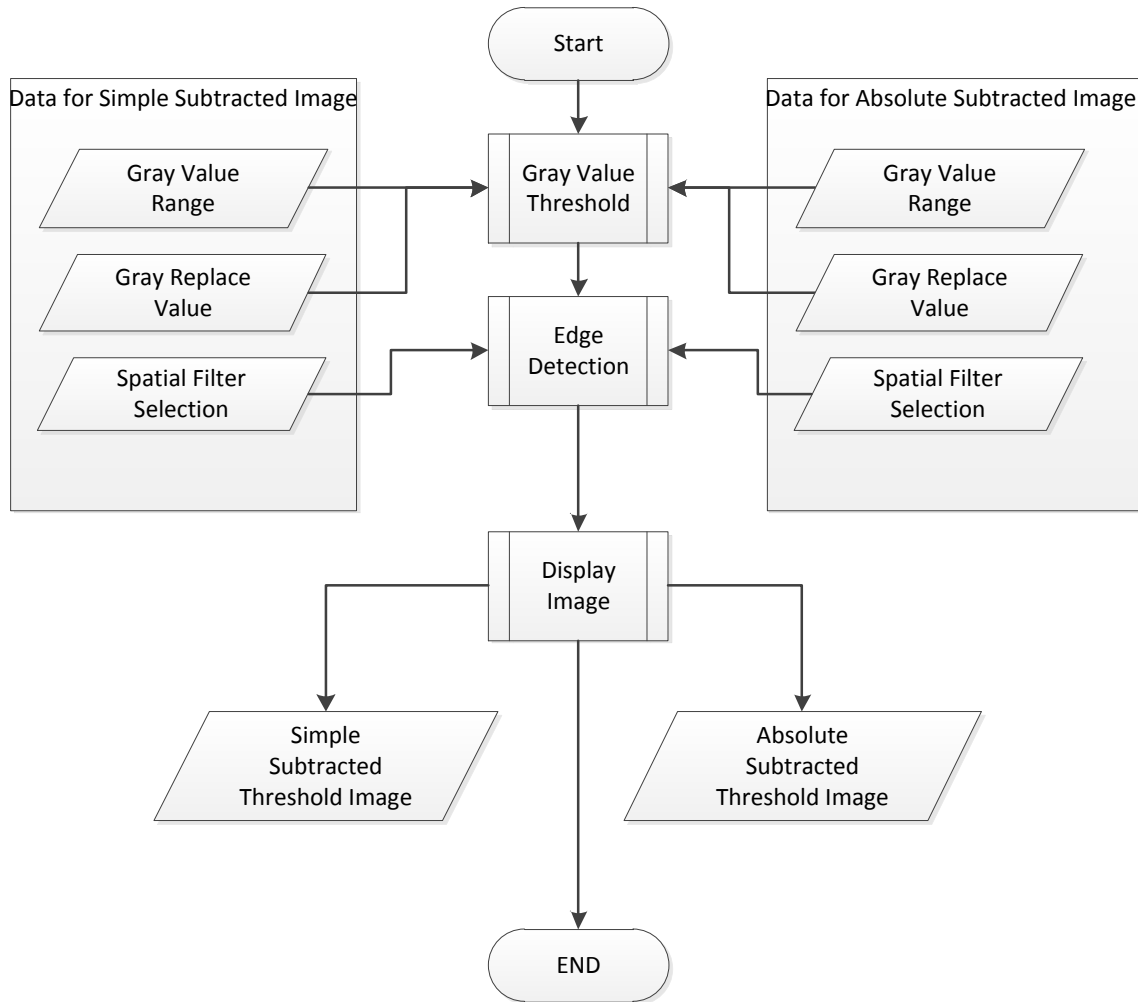


Figure 42. Image edges detection process.

THIS PAGE INTENTIONALLY LEFT BLANK

## APPENDIX B. APPLICATION SOFTWARE HMI

The interface shown in Figure 43 was built to provide an easy operation of all camera controls and an interactive manipulation of the images displayed to the user.

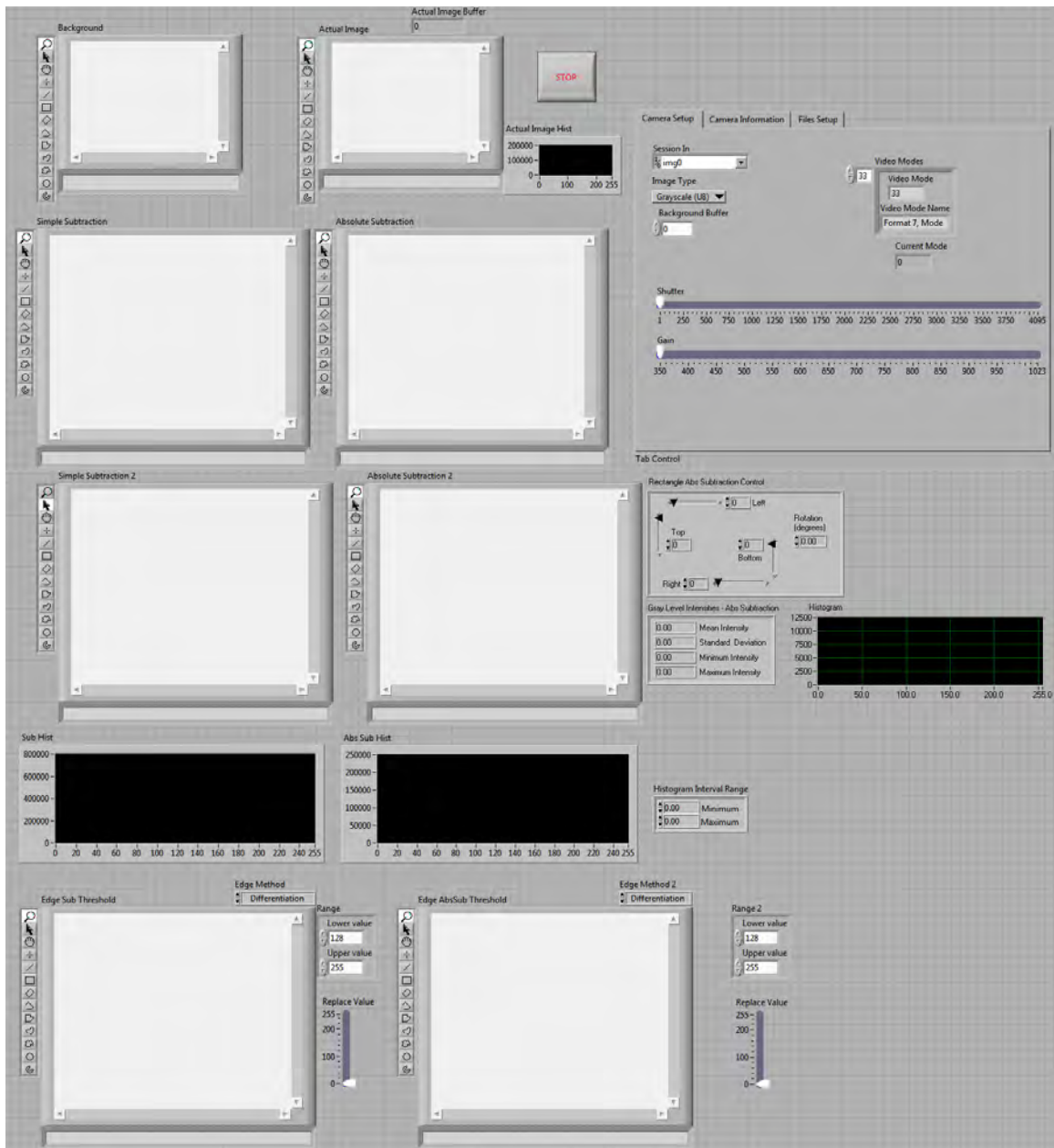


Figure 43. Software application front panel.

THIS PAGE INTENTIONALLY LEFT BLANK

## APPENDIX C. APPLICATION BLOCK DIAGRAM

The software was developed using the LabView development tools which permit the implementation of functions and scripts in a high-level visualization using icons and blocks. All necessary functions were implemented in separated sub-blocks that are executed in a fixed logical sequence. The first sub-block in the execution sequence is depicted in Figure 44 and is responsible for configuring the camera with some chosen parameter attributes.

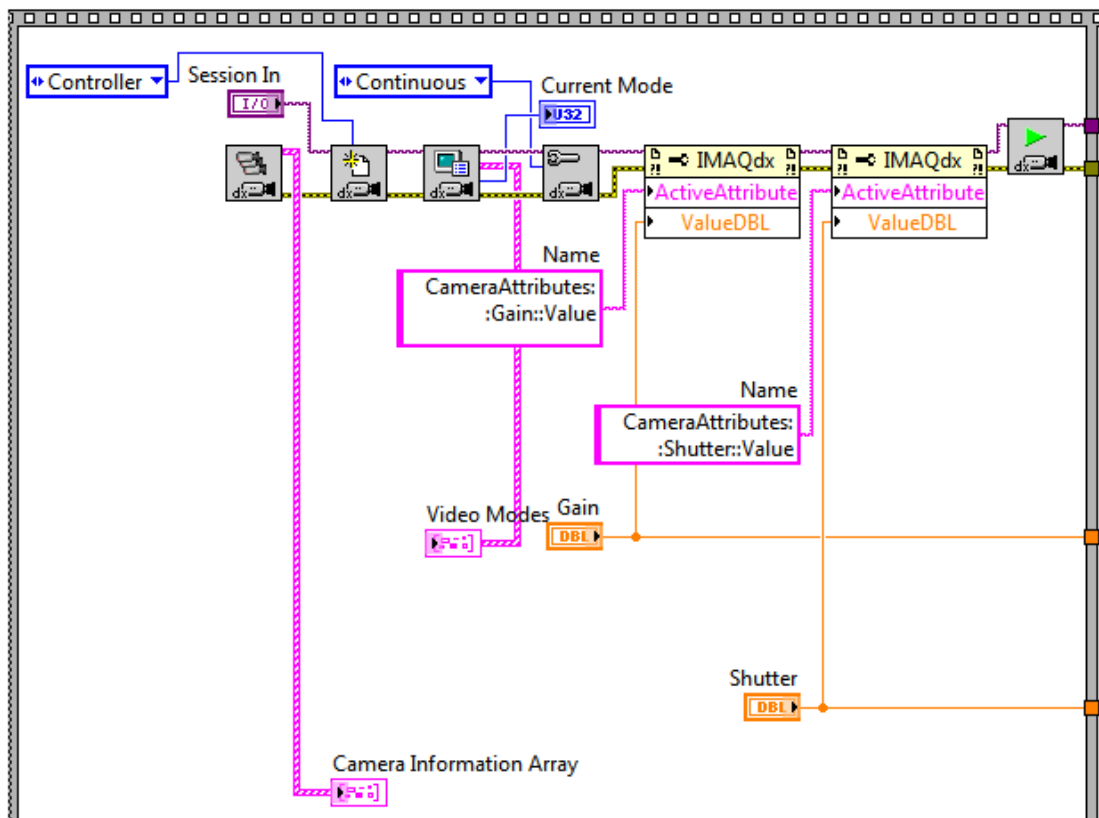


Figure 44. First sub-block diagram.

The second sub-block (Figure 45) executes the acquisition of the background reference image.

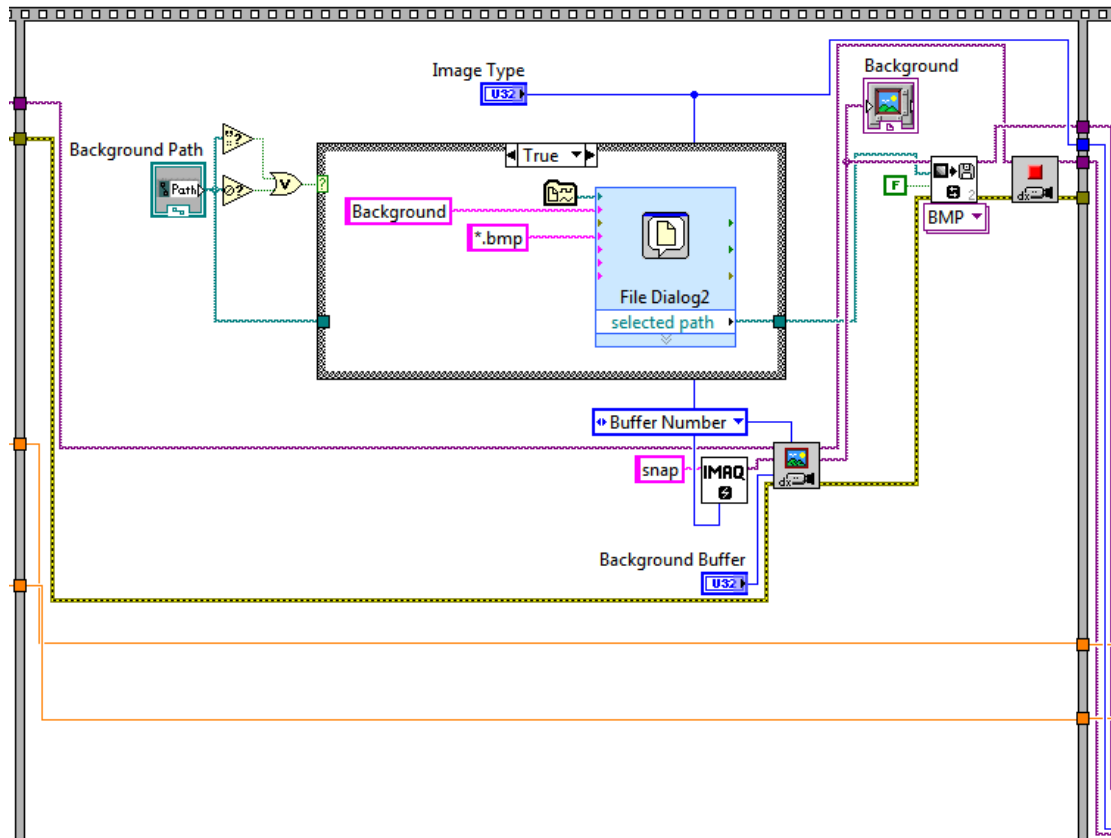


Figure 45. Second sub-block diagram.

The third sub-block (Figure 46) is the most complex of the software, and executes frames acquisition and information display continuously until the user gives a “stop” event.



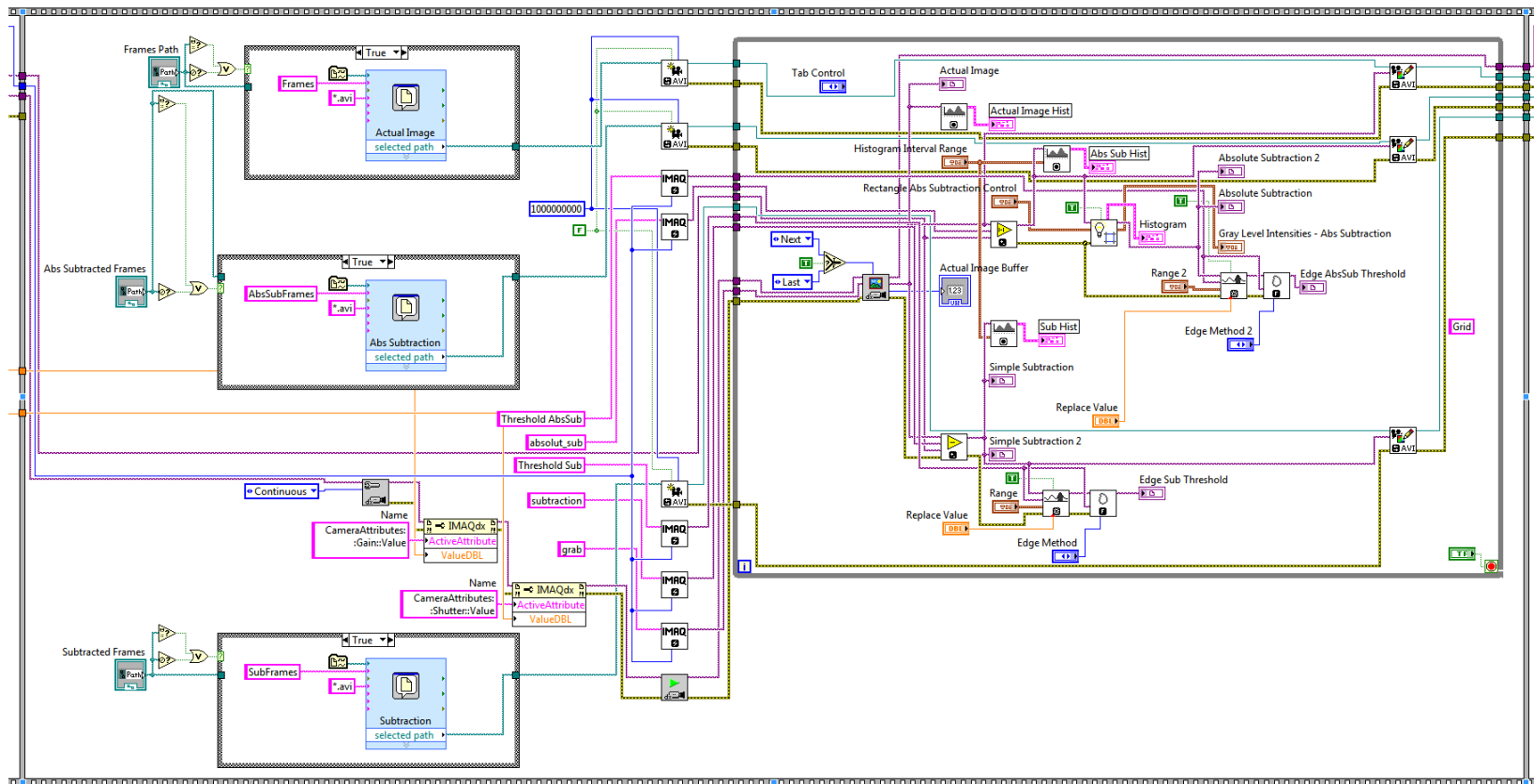


Figure 46. Third sub-block diagram.

The last sub-block (Figure 47) contains software functions necessary to stop the software execution without logical errors. Thus, it does not implement any process described in Appendix B.

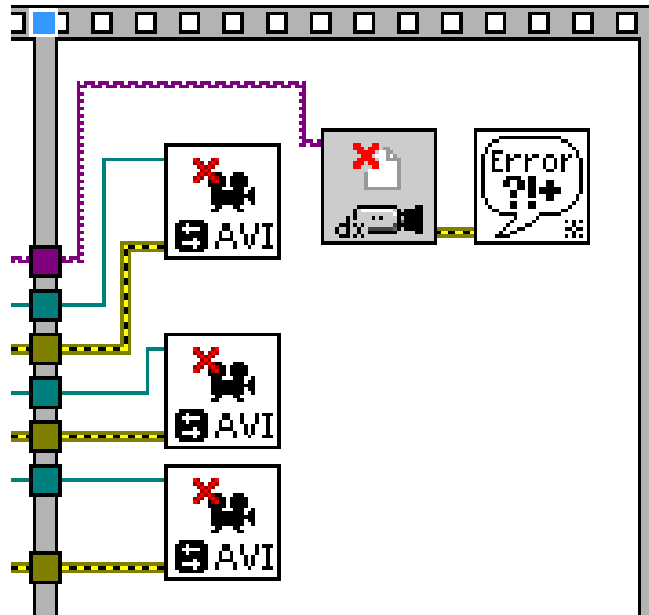


Figure 47. Fourth sub-block diagram.

## INITIAL DISTRIBUTION LIST

1. Defense Technical Information Center  
Ft. Belvoir, Virginia
2. Dudley Knox Library  
Naval Postgraduate School  
Monterey, California
3. Prof. Dragoslav Grbovic  
Naval Postgraduate School  
Monterey, California
4. Prof. David C. Jenn  
Naval Postgraduate School  
Monterey, California
5. Dr. Fabio Durante Pereira Alves  
Naval Postgraduate School  
Monterey, California
6. Prof. Gamani Karunasiri  
Naval Postgraduate School  
Monterey, California
7. Dan C. Boger  
Naval Postgraduate School  
Monterey, California